Recuperators and Regenerators in Supercritical Carbon Dioxide Power Cycles

by

Katheryn Yoder

A thesis submitted in partial fulfillment of

the requirements for the degree of

Master of Science

(Mechanical Engineering)

at the

UNIVERSITY OF WISCONSIN-MADISON

2015

This thesis has been approved by

_____

Professor Sanford A. Klein

_____

Professor Gregory F. Nellis

_____

Professor Mark H. Anderson

Date: _____

Abstract

Heat exchangers play a pivotal role in the cost of S-CO2 power cycles. Previous studies have suggested that the printed circuit heat exchanger (PCHE) is the ideal recuperator for this cycle because of its compact size and thus its reduced cost compared to an equivalent shell and tube heat exchanger. Nevertheless, the PCHE must be manufactured using expensive high grade alloys. While several researchers have compared PCHEs to other forms of indirect heat exchangers, none of them have explored the possibility of utilizing a direct heat exchanger within an S-CO2 power cycle. A compact direct heat exchanger can be constructed using inexpensive materials without requiring large, complex joint areas.

This paper examines a direct form of reheating known as a fixed-bed regenerator in the context of an S-CO2 power cycle. Specifically, this study uses a numerical simulation implemented in the Engineering Equation Solver (EES) software to model a PCHE and an implicit numerical simulation in MATLAB to model a switched-bed regenerator. These models are then used to optimize the design of each heat exchanger for a simple S-CO2 power cycle with an electrical output of 10 MW. The effects of sphere size, cycle time, and carryover on the regenerator performance are all examined.

When comparing the size and cost of these two heat exchanger designs, it is found that the regenerator can result in a significant reduction of cost, upwards of 80% compared to the cost of an equivalent recuperator. The regenerator can also produce a 30%-50% reduction in volume if 1.59 mm (1/16”) or smaller diameter spheres are used in the packed bed. The overall geometries of these tanks are impractical for a two-tank system; a better method would be to divide the tanks into a series of smaller pipes. The number of these pipes

depends on both the effectiveness and the pressure ratio reduction across the turbine. When including carryover in the regenerator design, the effectiveness of the regenerator decreases by at least 13%, depending on the cycle time.

Overall, the regenerator can produce a significant advantage to heat recovery, especially in respect to cost. If designed correctly, the regenerator could also occupy a smaller area than the recuperator, which would expand these benefits to applications in which size is important. There are important aspects that need to be taken into account when designing a regenerator, especially carryover and the need for a multi-tank system. These areas need to be researched further before a definitive conclusion about the regenerator's advantage can be made.

Acknowledgements

First I'd like to thank my advisors Sanford Klein, Gregory Nellis, as well as Mark Anderson for their guidance and support. Because of them, my abilities as an engineer and a scientist have greatly improved, and I could not have completed this project without their knowledge and motivation.

I'd also like to thank my parents, who have been nothing but supportive during my time in graduate school. They are the reason I decided to study mechanic-al engineering, and I could not have gotten this far without their encouragement.

Finally, I would like to thank John E., John D., Wenjie, Kelsey, Allie, Joe, Avi, Evan, and the rest of the SEL group for their friendship and support. Thanks for spending your days with me; I will certainly miss you all and I hope I'll see you all again in the future.

Table of Contents

Table of Figures

List of Tables

Nomenclature

Abbreviations

PCHE	Printed Circuit Heat Exchanger
SCO_2	Supercritical Carbon Dioxide
CSP	Concentrating Solar Power
EES	Engineering Equation Solver (Software)
Sandia	Sandia National Laboratories
DOE-NE	Department of Energy Office of Nuclear Energy
HT	High Temperature
LT	Low Temperature
316 SS	316 stainless steel

Variables

UA	Conductance
T	Temperature
ε	effectiveness
Q	Heat transfer rate
W	Work
h	Enthalpy
m	Mass flow rate
N	Number of sub-HX's
C	Capacitance rate
NTU	Number of transfer units
C_r	Capacitance Ratio
s	Entropy
P	Pressure
cp	Specific heat at constant pressure
cv	Specific heat at constant volume
Nu	Nusselt Number
Re	Reynolds Number
Pr	Prandtl Number
D	Diameter
Dh	Hydraulic diameter
t_{wall}	Thickness of plate
t_H	Hot fluid channel height
t_C	Cold fluid channel height
t_{fin}	Fin thickness
Width	Channel width
Width_HX	Recuperator width
Height_HX	Recuperator height
Length	Recuperator length
N_{fins}	Number of fins

N_{ch}	Number of channels
N_{pair}	Number of pairs of rows
A_c	Cross sectional area
Per	Perimeter of channel
vel	Fluid velocity
μ	Fluid viscosity
ρ	Fluid density
f	Friction factor
R_{conv}	Convection resistance
R_{cond}	Conduction resistance
R_{fin}	Fin resistance
η_{fin}	Fin efficiency
η_o	Overall fin efficiency
η	Efficiency
I	inertia
V	Shear force
M	Bending moment
σ	Bending stress
τ	Shear stress
h_{conv}	Heat transfer coefficient
k	Thermal conductivity
Vol	volume
φ	porosity
A_s	Surface area
t_b	Cycle time
α_s	specific surface area
Π	reduced time
Λ	reduced length
U	utilization factor
Bi	Biot number
C_d	Discharge coefficient

Subscripts

s	isentropic
h	hot side
c	cold side
max	Maximum
min	Minimum
in	Inlet
out	Outlet
i	node position through space
j	node position through time

eq	equivalent
m	mean
HX	recuperator
f	fluid
r	regenerator material
HTCB	hot to cold blow
CTHB	cold to hot blow
ch	channel

1 Introduction

1.1 Motivation

The demand for clean, renewable energy has increased over the years as more consumers find the environmental and economic benefits of such eco-friendly sources more appealing. In addition to reducing dependence on foreign oil, renewable energy can also encourage economic development by creating jobs in manufacturing, installation, and other important areas (Renewable Energy 2013). With a price reduction of around 25% in the past five years (Solar Energy in Demand 2012), solar energy in particular is growing as a viable form of alternative energy.

There are several ways in which solar energy can be used to produce electricity. The most common method converts solar radiation directly into electricity through the use of photovoltaic cells. Such devices are typically known as solar panels and are used in both residential and commercial applications. The second method transfers the thermal energy from the sun into the working fluid of a conventional power cycle; this technique is more efficient and economical for large scale power generation than solar panels (Feierabend 2009).

One of the downsides of using solar energy is that a lot more space is required to produce electricity compared to plants that use coal or natural gas. For example, in Vineyard, Utah, two combined-cycle natural gas power plants known as Lake Side I and II sit on 65 acres of land; together they can generate 1.2 GW_e (Lake Side Generation Facilities 2014). On the other hand Ivenpah, a solar plant situated in the Mojave desert, is designed to produce 377 MWe, but its collector fields and receiving towers cover a span of 3500 acres (Ivenpah Facts

2013). One of the largest concentrating solar power (CSP) plant in the world produces 1/3 of the electricity of those natural gas plants while covering over 50 times the area. This large area requirement limits the use of solar plants to places like deserts, which cover less than 10% of the continental U.S.

1.2 S-CO_2 Brayton Cycles

One of the solutions to the issue of space is to replace the steam cycle with a supercritical one. A basic closed Brayton cycle, or closed gas turbine, consists of four components: a compressor, a turbine, and two heat exchangers (Figure 1.1).

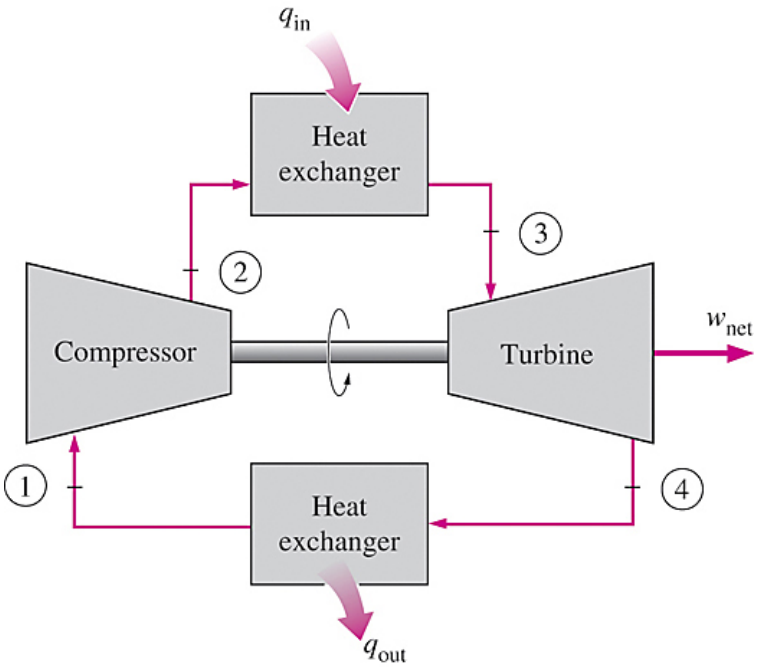

Figure 1.1: Example of closed gas turbine cycle (Çengel 2010)

The working fluid is heated using the primary heat exchanger before moving through the turbine, which both operates the compressor and generates electricity via a generator. The fluid then moves through the precooler, which removes waste heat before the fluid travels

through the compressor. Some cycles also include a recuperator, which helps recover waste heat and increases the efficiency of the system.

Closed Brayton were first used for commercial power generation in Germany in the 1930s. These plants used air as the working fluid, and many remained in operation until the 1970s (Keller, 1978). The success of air-based turbines inspired the development of the helium gas closed Brayton cycle, which was built around 1963 in the United States and soon used in nuclear power generation (La Fleur 1963). Though engineers recognized that the closed gas turbine could be used with other working fluids such as nitrogen and carbon oxide, helium was still considered the most useful for larger plants (Keller, 1978). As technology has advanced, however, supercritical fluid has become an interesting alternative to other working fluids.

The term "supercritical" refers to a fluid's state once its pressure and temperature exceed the critical point (Figure 1.2). For carbon dioxide, the critical temperature is about 31°C (88°F) and the critical pressure is about 7.4 MPa (1071 psia).

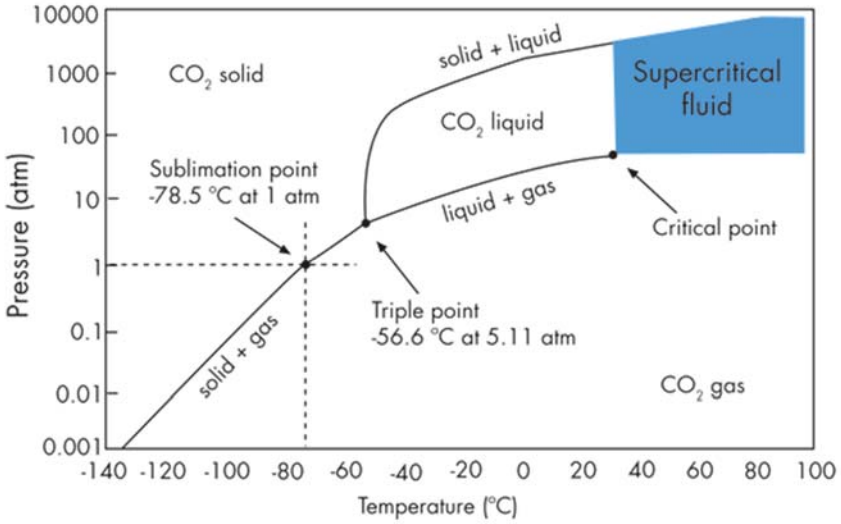

Figure 1.2: Phase diagram for carbon dioxide (Hunter 2010).

In the supercritical region, distinct liquid and gas phases do not exist. Supercritical fluids have the low viscosity of a gas and the high density of a liquid, and these properties are highly dependent on temperature and pressure (Figure 1.3).

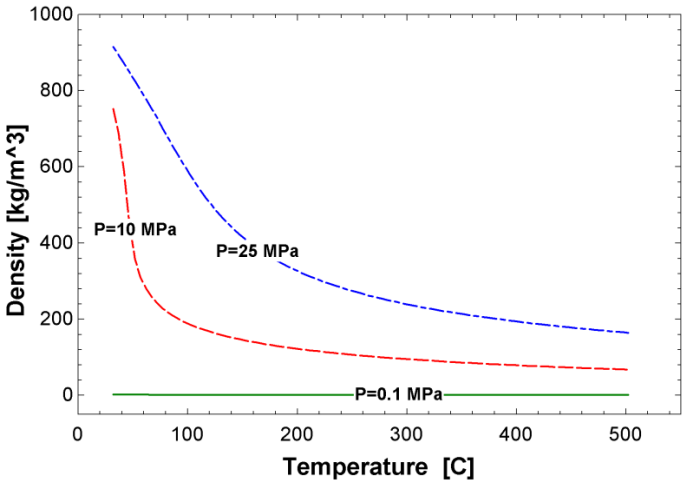

Figure 1.3: Plot of carbon dioxide density both above and below the critical point.

Because carbon dioxide is so dense in its supercritical state, a closed cycle using supercritical carbon dioxide has a high power density. This means that the gas turbine can operate at about $1/10^{th}$ the cost and $1/100^{th}$ the plant volume of a typical steam plant (Pasch 2013). Figure 1.4 below shows that a smaller supercritical carbon dioxide (S-CO_2) turbine can still produce more work than either a helium or steam turbine.

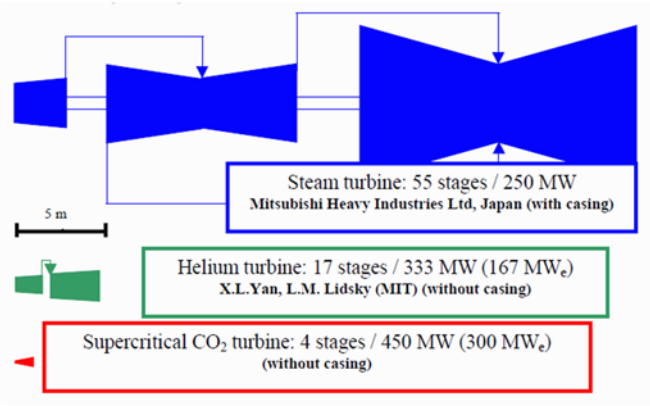

Figure 1.4: Size comparison of steam, helium, and S-CO_2 turbines (Dostal 2004).

1.3 Printed Circuit Heat Exchangers

To help recover waste heat and increase cycle efficiency, S-CO_2 power cycles typically include a recuperator in their design (Figure 1.5).

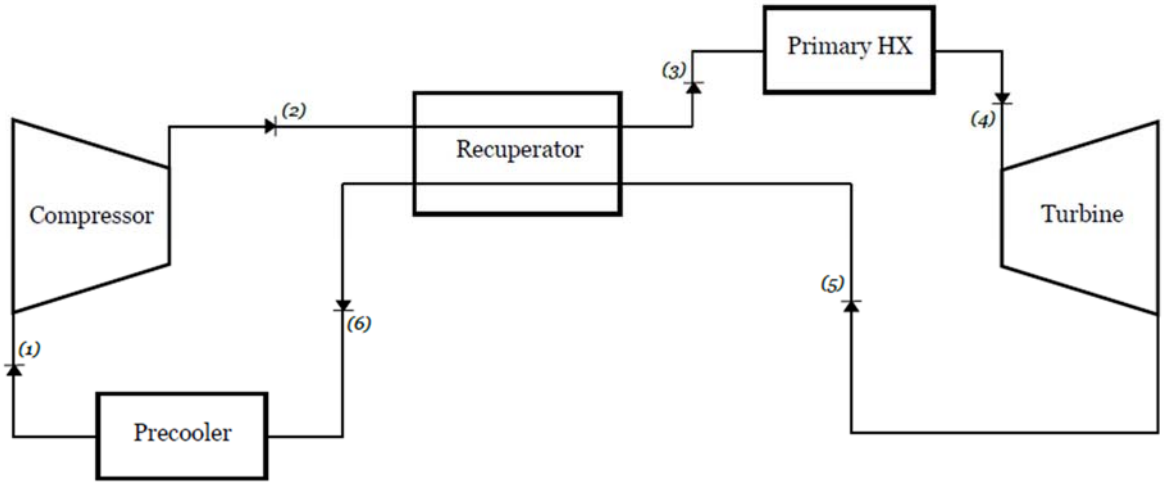

Figure 1.5: Simple S-CO2 cycle with recuperation.

The recuperator most often used is the Printed Circuit Heat Exchanger (PCHE), which was invented at the University of Sydney in the early 1980s (Li, 2011). PCHEs are manufactured by chemically etching flow channels onto a series of plates that are then joined together using diffusion bonding. The use of diffusion bonding allows the PCHEs to operate over a wide range of pressures and temperatures, and they have a longer lifespan than any other heat exchanger (Li 2011). These heat exchangers are popular because of their high specific surface area, which makes them more compact than a typical shell-and-tube heat exchanger (Figure 1.6).

Figure 1.6: Comparison of PCHE (foreground) and equivalent shell and tube exchanger for a 4MW cooling duty (Heatric).

Heatric, a company based in the UK, began producing these heat exchangers commercially in 1985, and since then over 1,000 units have been sold, with many still in operation today (Le Pierres 2011). PCHEs are most commonly used in the hydrocarbon processing industry and the upstream oil and gas market. More recently engineers have begun using PCHEs in cryogenic and nuclear application, where compactness is crucial for heat exchangers (Van Meter 2008). PCHEs are preferred for S-CO_2 power cycles because of their small size and ability to withstand extreme operating conditions, but they are very expensive, contributing to the majority of the cycle cost.

1.4 Regenerators

A potentially cheaper alternative for recovering waste heat is the regenerator, which utilizes a compact matrix with high heat capacity to indirectly transfer energy between streams. The first regenerator was invented by Robert Stirling in 1816, and later became a component of his Stirling engine. This was a type of fixed bed regenerator, in which a single fluid stream has a cyclical, reversible flow through a matrix bed. Fixed bed regenerators can also consist

of two stationary beds and a valve system that switches the hot and cold fluid streams between them (Figure 1.7).

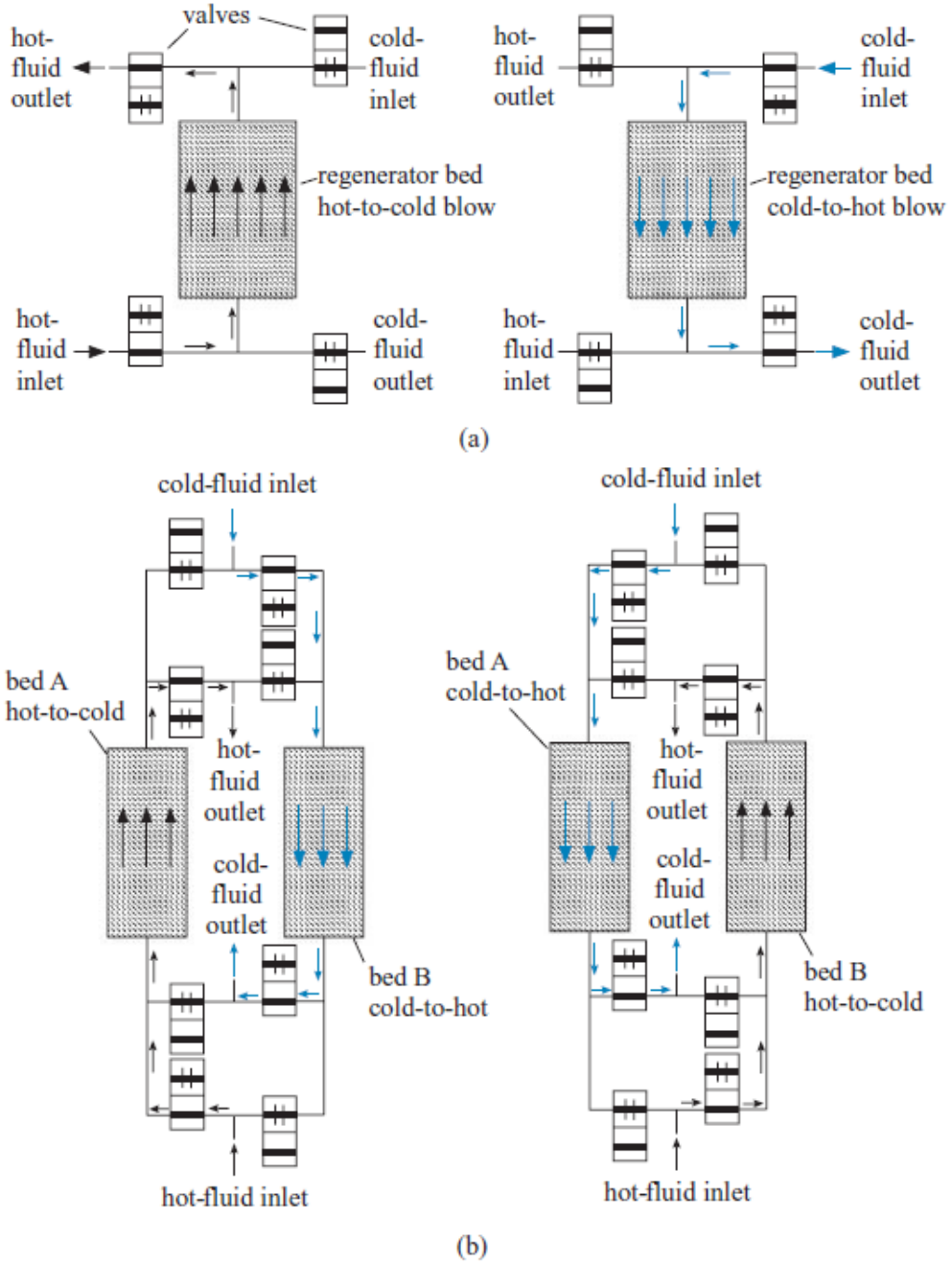

Figure 1.7: Diagram of (a) single bed and (b) double bed fixed regenerators (Nellis, 2012)

A rotary regenerator, first proposed by Nusselt in 1927, consists of two streams that pass through a rotating wheel (Figure 1.8). Nusselt's theories were expanded by several people in the 1930s and early 1940s, but no working rotary regenerator was made or tested until after WWII (Cox 1950).

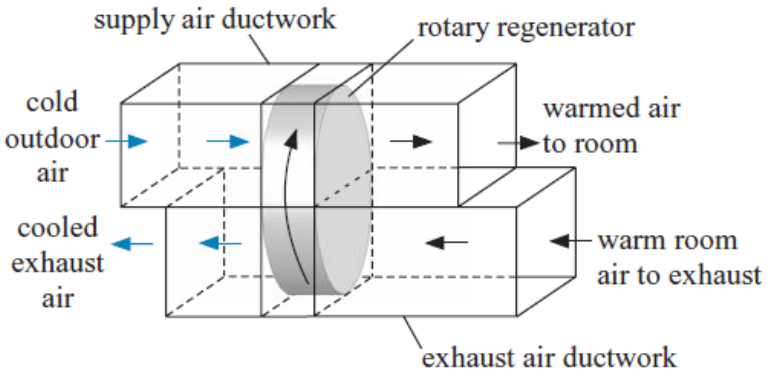

Figure 1.8: Diagram of rotary regenerator (Nellis 2012).

These regenerators, especially the rotary type, were originally used in the steel industry to recover heat from waste gases, and their uses have expanded to include cryogenics, desiccants, and dehumidifiers, and gas turbine power plants in order to improve specific fuel consumption (Cox 1950). The matrix material used in the regenerator has a high specific surface area, which, like the PCHE, results in a more compact device compared to the shell-and-tube heat exchanger, but the main concern with regenerators is leakage (Skiepko 2004).

For a fixed bed regenerator, leakage can come from two main sources; carryover, which is defined as the interstitial fluid that remains in the regenerator matrix and pipes at the end of a period. This fluid is removed when the new stream flows through the matrix, but the net result is a leakage loss in the regenerator. The second leakage is pressure leakage, which occurs as the valves switch hot and cold streams. This leakage always occurs from high to low pressure; in this case it always leaks from the cold to the hot flow. The valve leakage

rate depends on the discharge coefficient and the valve area, both of which depend on the type of valve being used. According to Skiepko, these leakages can be significant, and should be examined in-depth in order to determine their effect on performance.

1.5 Objectives

While a lot of research has gone into printed circuit heat exchangers, especially its thermal and hydraulic performance given different channel types (Ngo et al. 2006; Tsuzuki et al. 2007; Nikitin et al. 2006; Kim et al. 2008; Pra et al. 2008)), no substantial research has been done for regenerators in S-CO_2 applications. Given that regenerators are simpler to manufacture, there could be a large cost benefit to using one instead of a traditional recuperator.

The objective of this work is to explore the use of a switched bed regenerator in a simple S-CO_2 power cycle. Specifically, this study compares the size and cost of a PCHE and a regenerator designed to operate in a simple S-CO_2 power cycle with an electrical output of 10 MW. This study also investigates the limitations of the switch bed regenerator by exploring the effects of carryover and other forms of leakage.

2 Computational Model of PCHE

Before the feasibility of the fixed bed regenerator can be determined, it must be compared to a printed circuit heat exchanger (PCHE) that has the same performance. This chapter outlines the method behind the PCHE model; the results are discussed in Chapter 3.

2.1 Cycle Analysis

A counter-flow recuperator is required for a simple closed Brayton Cycle, which is comprised also of one compressor and one turbine, a primary heat exchanger, and a precooler (Figure 2.1: Diagram of a simple Brayton cycle. The numbers in italics reference various points in the cycle.).

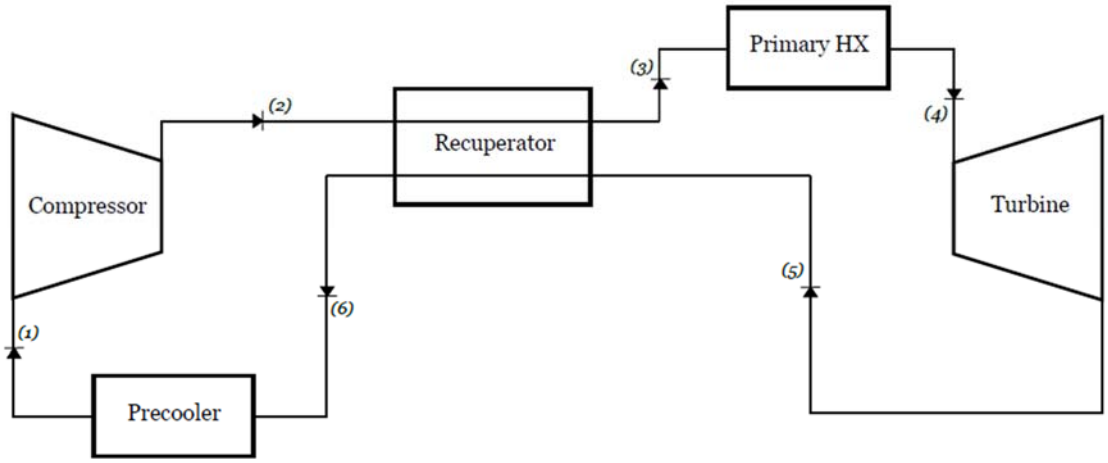

Figure 2.1: Diagram of a simple Brayton cycle. The numbers in italics reference various points in the cycle.

The temperature and pressure at the compressor inlet (State 1) are provided. The density ρ_1 of carbon dioxide is calculated based on the temperature and pressure at state 1 using Engineering Equation Solver (EES, Klein, 2015). The specific enthalpy h_1 and entropy s_1, are also found using EES. By assuming that the compressor is isentropic, the ideal outlet specific enthalpy $h_{s,2}$, is found in a similar manner using s_1 and P_2. The mass flow rate $\dot{m}$ is

specified, so the isentropic work done by the compressor $\dot{W}_{s,c}$ can be calculated using the first law of thermodynamics.

$$\dot{W}_{s,c} = \dot{m}\left(h_1 - h_{s,2}\right) \tag{2.1}$$

The compressor does not operate isentropically, so the actual work $\dot{W}_c$ is calculated based on its efficiency η_c according to:

$$\eta_c = \frac{\dot{W}_{s,c}}{\dot{W}_c} \tag{2.2}$$

The actual compressor work is used to calculate the actual specific enthalpy at state 2 h_2 Once the enthalpy is known, the temperature and specific entropy is found using EES.

$$\dot{W}_c = \dot{m}\left(h_1 - h_2\right) \tag{2.3}$$

The turbine is analyzed in a similar manner. The temperature and pressure at state 4 are used to find the specific enthalpy h_4 and entropy s_4. These properties are then used to determine the isentropic and actual turbine work.

$$\dot{W}_{s,t} = \dot{m}\left(h_4 - h_{s,5}\right) \tag{2.4}$$

$$\eta_t = \frac{\dot{W}_t}{\dot{W}_{s,t}} \tag{2.5}$$

$$\dot{W}_t = \dot{m}\left(h_4 - h_5\right) \tag{2.6}$$

The work $\dot{W}_c$ needed by the compressor is negative, and the work $\dot{W}_t$ generated by the turbine is positive. Since some of the energy produced by the turbine is used to operate the compressor, the net work $\dot{W}_{net}$ that is produced by the generator is calculated based on the actual turbine and actual compressor work.

$$\dot{W}_{net} = \dot{W}_t + \dot{W}_c \tag{2.7}$$

2.2 Recuperator Analysis

The recuperator is designed so that both the hot and cold channels have the same channel width and heights t_h and t_c (Figure 2.2). The number of channels on the hot side and the cold side are adjusted in order to achieve a specified pressure drop.

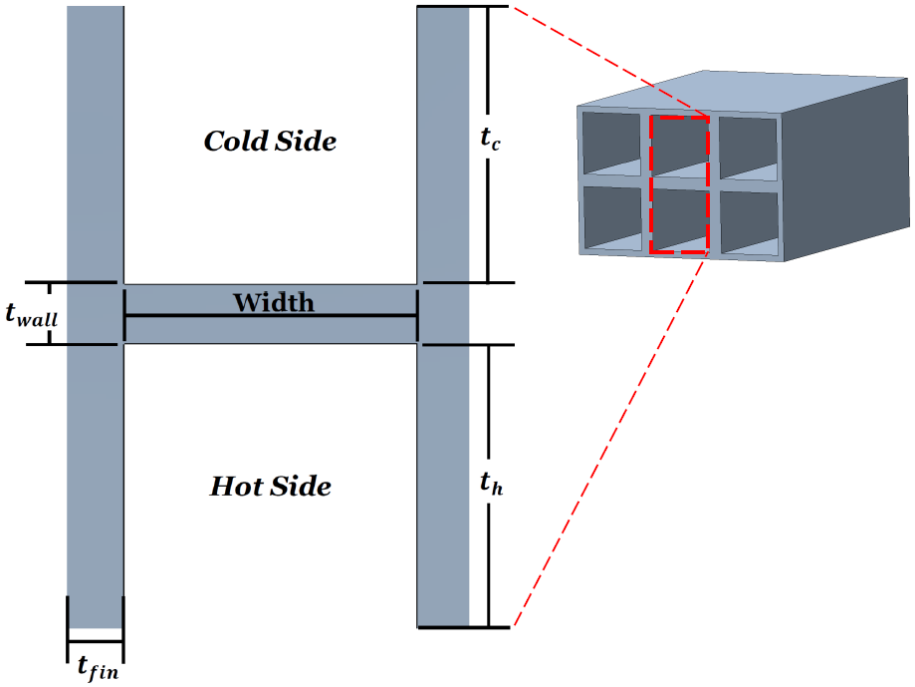

Figure 2.2: Diagram of a modeled PCHE section. The notations for the channel dimensions are shown in the zoomed-in section.

The smallest section of the recuperator that is analyzed is referred to as a unit cell (Figure 2.3). The results obtained from the analysis of a unit cell are scaled in order to represent the results for the entire recuperator. Two unit cells form the equivalent of one channel pair.

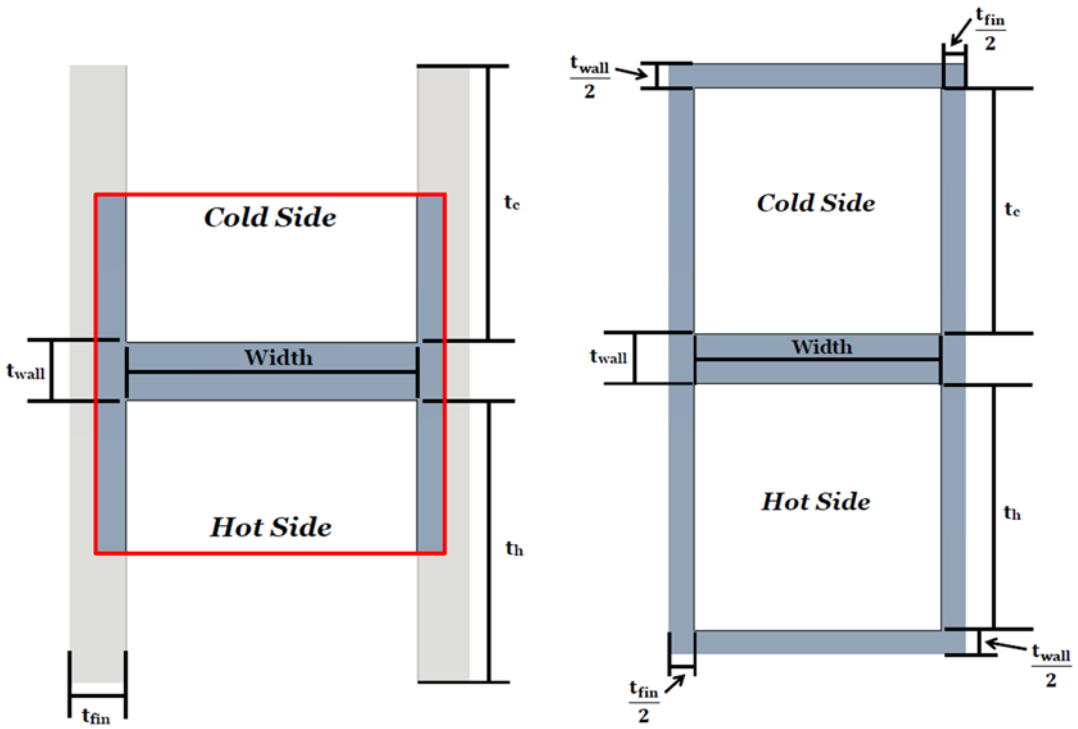

(a) **(b)**

Figure 2.3: Example of (a) a unit cell and (b) a channel pair. One channel pair is the equivalent of two unit cells.

The number of fins that are in one row of hot channels $N_{fin,h}$ and one row of cold channels $N_{fin,c}$ are both evaluated based on the overall width of the recuperator $Width_{HX}$ in Eq. (2.8) and (2.9). In Eq. (2.10), the overall height $Height_{HX}$ is used to find the number of pairs of rows N_{pair}. The total number of channels on the hot side $N_{ch,h}$ and the cold side $N_{ch,c}$ are then calculated based on $N_{fin,h}$, $N_{fin,c}$, and N_{pair} in Eq. (2.11) and (2.12).

$$Width_{HX} = Width\left(N_{fin,h}+1\right)+t_{fin,h}\left(N_{fin,h}+2\right) \tag{2.8}$$

$$Width_{HX} = Width\left(N_{fin,c}+1\right)+t_{fin,c}\left(N_{fin,c}+2\right) \tag{2.9}$$

$$Height_{HX} = N_{pair}\left(2t_{wall}+t_h+t_c\right)+t_{wall} \tag{2.10}$$

$$N_{ch,h} = 2N_{pair}\left(N_{fin,h}+1\right) \tag{2.11}$$

$$N_{ch,c} = 2N_{pair}\left(N_{fin,c}+1\right) \tag{2.12}$$

Since the fluid is diverted into small channels as it flows through the recuperator, the mass flow rate through each channel is evaluated by dividing the total mass flow rate by the number of channels on each side.

$$\dot{m}_{ch,h} = \frac{\dot{m}}{N_{ch,h}} \tag{2.13}$$

$$\dot{m}_{ch,c} = \frac{\dot{m}}{N_{ch,c}} \tag{2.14}$$

The total energy transfer rate $\dot{Q}_{regen}$ across the recuperator is specified to meet the system's performance requirements. The inlet temperature on the hot side $T_{h,in}$ is known based on the cycle analysis, so the hot side outlet temperature $T_{h,out}$ is calculated based on the hot side energy balance.

$$\dot{Q}_{regen} = \dot{m}\left(h_{h,in} - h_{h,out}\right) \tag{2.15}$$

Once $h_{h,out}$ is known, $T_{h,out}$ can be calculated using EES. It is assumed that there is no heat loss from the jacket of the recuperator; therefore the heat transferred to the cold side (states 2-3) must equal the heat transferred from the hot side (states 5-6). The enthalpy $h_{c,out}$ at the cold side outlet is calculated based on this information.

$$\dot{Q}_{regen} = \dot{m}\left(h_{c,out} - h_{c,in}\right) \tag{2.16}$$

The outlet temperature on the cold side of the recuperator is then evaluated based on $h_{c,out}$ and the corresponding pressure at that point in the cycle. The cold side inlet temperature $T_{c,in}$, and thus the inlet enthalpy $h_{c,in}$, is known from the cycle analysis.

Because the properties of carbon dioxide vary significantly across the recuperator, it must be divided into several smaller heat exchangers along the flow direction (Figure 2.4). The properties are assumed to be constant across each sub-HX.

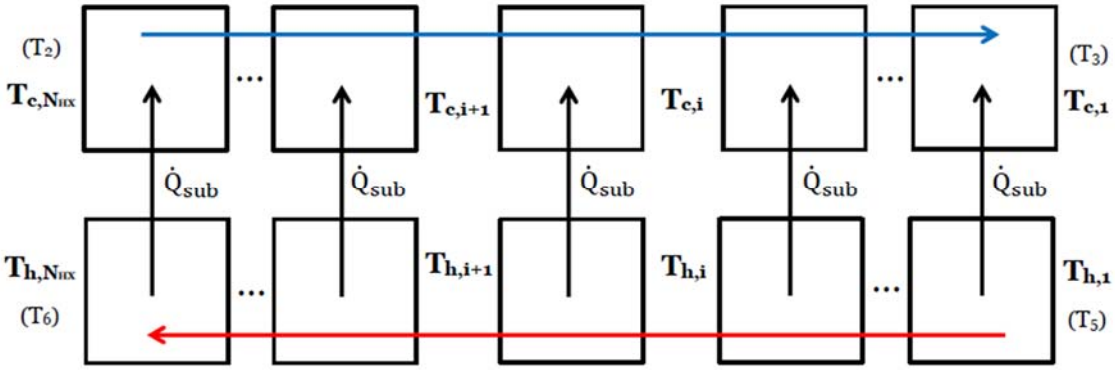

Figure 2.4: Diagram of sub-heat exchangers. Temperatures Th,1 and Th,NHX refer to the temperatures at the hot side inlet (state 5) and hot side outlet (state 6), respectively. Temperature Tc,1 refers to the temperature at the cold side outlet (state 3) and Tc,NHX refers to the temperature at the cold side inlet (state 2).

First, the total heat transfer rate $\dot{Q}_{regen}$ is divided by the number of sub-heat exchangers N_{HX} needed to calculate the heat transfer rate through each sub-HX.

$$\dot{Q}_{sub} = \frac{\dot{Q}_{regen}}{N_{HX}} \tag{2.17}$$

This heat transfer rate is then used with enthalpies $h_{h,i}$ and $h_{c,i}$ at the initial end of the sub-HX to find the hot and cold side enthalpies $h_{h,i+1}$ and $h_{c,i+1}$ on the opposite end (see Figure 2.4).

$$h_{h,i+1} = h_{h,i} - \frac{\dot{Q}_{sub}}{\dot{m}} \tag{2.18}$$

$$h_{c,i+1} = h_{c,i} - \frac{\dot{Q}_{sub}}{\dot{m}} \tag{2.19}$$

Temperatures $T_{h,i+1}$ and $T_{c,i+1}$, along with entropies $s_{h,i+1}$ and $s_{c,i+1}$, are found also found at those locations based on the enthalpies and pressures.

2.3 Fluid Properties

The fluid properties across one sub-HX are found by taking the average temperature across the hot side $T_{m,h}$ and cold side $T_{m,c}$.

$$T_{m,h,i} = \frac{T_{h,\,i} + T_{h,\,i+1}}{2} \tag{2.20}$$

$$T_{m,c,i} = \frac{T_{c,\,i} + T_{c,\,i+1}}{2} \tag{2.21}$$

Fluid densities $\rho_{h,i}$ and $\rho_{c,i}$ are used to calculate the velocities $vel_{h,i}$ and $vel_{c,i}$, which are in turn used to solve for Reynolds numbers $Re_{h,i}$ and $Re_{c,i}$. The flow through the PCHE used in this study is turbulent.

$$vel_{h,i} = \frac{\dot{m}_{ch,h}}{\rho_{h,i}\ A_{cross,h}} \tag{2.22}$$

$$Re_{h,i} = \frac{\rho_{h,i}\ vel_{h,i}\ D_{h,h}}{\mu_{h,i}} \tag{2.23}$$

$$vel_{c,i} = \frac{\dot{m}_{ch,c}}{\rho_{c,i}\ A_{cross,c}} \tag{2.24}$$

$$Re_{c,i} = \frac{\rho_{c,i}\ vel_{c,i}\ D_{c,h}}{\mu_{c,i}} \tag{2.25}$$

The hydraulic diameter of the hot side $D_{h,h}$ and cold side $D_{h,c}$ were calculated based the dimensions of each channel. The variable A_{cross} refers to the cross-sectional area of the channel, while Per refers to the perimeter.

$$D_{h,h} = \frac{4A_{cross,h}}{Per_h} \tag{2.26}$$

$$D_{h,c} = \frac{4 A_{cross,c}}{Per_c} \tag{2.27}$$

$$A_{cross,h} = t_h \left(Width\right) \tag{2.28}$$

$$Per_h = 2(t_h + Width) \tag{2.29}$$

$$A_{cross,c} = t_c \left(Width\right) \tag{2.30}$$

$$Per_c = 2(t_c + Width) \tag{2.31}$$

The DuctFlow function in EES solves for the Nusselt Number and the friction factor *f*, given the Reynolds number *Re*, Prandtl number *Pr*, the ratio *L/D* of length to hydraulic diameter, aspect ratio, and relative roughness of the channel. *L/D* was set to a very large value because the flow is assumed to be fully developed, and the relative roughness was set to zero because the channel is assumed to be smooth.

The Nusselt number, the hydraulic diameter, D_h, and the conductivity of the fluid in both the hot and cold channels were used to solve for the convection coefficients $h_{conv,h,i}$ and $h_{conv,c,i}$.

$$Nu_{h,i} = \frac{h_{conv,h,i} \; D_{h,h}}{k_{h,i}} \tag{2.32}$$

$$Nu_{c,i} = \frac{h_{conv,c,i} \; D_{h,c}}{k_{c,i}} \tag{2.33}$$

The pressure drop across each sub-HX is calculated based on the friction factor from the DuctFlow function.

$$f_{h,i} = -\left(\frac{dP}{dx}\right)_{h,i} \frac{2 \; D_{h,h}}{\rho_{h,i} \; vel_{h,i}^2} \tag{2.34}$$

$$f_{c,i} = -\left(\frac{dP}{dx}\right)_{c,i} \frac{2 \; D_{h,c}}{\rho_{c,i} \; vel_{c,i}^2} \tag{2.35}$$

The total pressure drop across the recuperator is then found by adding the pressure drops across each sub-heat exchanger.

$$dP_{h,tot} = \sum_{i=1}^{N_{HX}} \left(\frac{dP}{dx} \right)_{h,i} dx_i \tag{2.36}$$

$$dP_{c,tot} = \sum_{i=1}^{N_{HX}} \left(\frac{dP}{dx} \right)_{c,i} dx_i \tag{2.37}$$

2.4 Recuperator Conductance

Once the temperature distribution through the recuperator is known, the effectiveness-NTU method is used to determine the conductance of each sub-HX. The heat capacity rates of the hot side $C_{h,i}$ and the cold side $C_{c,i}$ are both found by multiplying the mass flow rate and the average heat capacity across each sub-HX.

$$C_{h,i} = \dot{m} \left(\frac{h_{h,i} - h_{h,i+1}}{T_{h,i} - T_{h,i+1}} \right) \tag{2.38}$$

$$C_{c,i} = \dot{m} \left(\frac{h_{c,i} - h_{c,i+1}}{T_{c,i} - T_{c,i+1}} \right) \tag{2.39}$$

These heat capacity rates are then used to calculate the maximum energy transfer rate across the recuperator.

$$\dot{Q}_{max,i} = \dot{C}_{min,i} \left(T_{h,i} - T_{c,i+1} \right) \tag{2.40}$$

The effectiveness $\varepsilon_{regen,i}$ is calculated using $\dot{Q}_{max,i}$ and $\dot{Q}_{sub}$.

$$\varepsilon_{regen,i} = \frac{\dot{Q}_{sub}}{\dot{Q}_{max,i}} \tag{2.41}$$

From here, the conductance of each sub-HX is evaluated based on the Number of Thermal Units (NTU).

$$NTU_i = \begin{cases} \dfrac{ln\left[\dfrac{1-\varepsilon_{regen,i}\ C_{R,i}}{1-\varepsilon_{regen,i}}\right]}{1-C_{R,i}} & for\ C_{R,i} < 1 \\ \dfrac{\varepsilon_{regen,i}}{1-\varepsilon_{regen,i}} & for\ C_{R,i} = 1 \end{cases} \tag{2.42}$$

$$C_{R,i} = \frac{\dot{C}_{min,i}}{\dot{C}_{max,i}} \tag{2.43}$$

$$UA_i = \dot{C}_{min,i}\ NTU_i \tag{2.44}$$

2.5 Recuperator Length

The concudctance can be related to the total thermal resistance $R_{tot,i}$ using Eq. (2.45).

$$\frac{UA_i}{2(N_{pair})} = \frac{1}{R_{tot,i}} \tag{2.45}$$

Since the number of hot and cold channels is not the same, $R_{tot,i}$ refers to the total resistance of one row of unit cells. This value is determined by first calculating the thermal resistance through one unit cell using a resistance network (Figure 2.5).

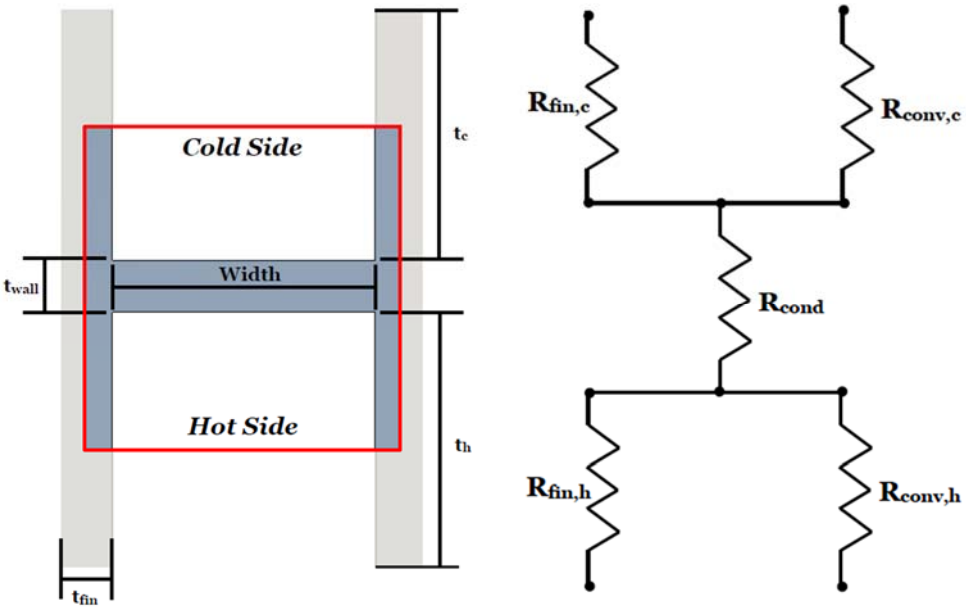

(a) **(b)**

Figure 2.5: Diagram of (a) a unit cell and (b) the thermal resistance through one unit cell.

The variable R_{fin} refers to the 1-d conduction through the side of the channel, which is modelled as a fin. Resistance R_{conv} refers to the heat transfer through the working fluid, and R_{cond} refers to the heat transfer through the material that separates the hot and cold channels. These thermal resistances are calculated using Eq. (2.46)−(2.50). The variable dx_i refers to the length of each sub-HX.

$$R_{conv,h,i} = \frac{1}{h_{conv,h,i}\left(Width\right)\left(dx_i\right)} \tag{2.46}$$

$$R_{conv,c,i} = \frac{1}{h_{conv,c,i}\left(Width\right)\left(dx_i\right)} \tag{2.47}$$

$$R_{cond,i} = \frac{t_{wall}}{k_{wall,i}\left(Width + t_{fin}\right)\left(dx_i\right)} \tag{2.48}$$

$$R_{fin,h,i} = \frac{1}{\eta_{h,i}\ h_{conv,h,i}\, 2\left(\frac{t_h}{2}\right)\left(dx_i\right)} \tag{2.49}$$

$$R_{fin,c,i} = \frac{1}{\eta_{c,i}\ h_{conv,c,i}\ 2\left(\frac{t_c}{2}\right)(dx_i)} \tag{2.50}$$

Fin efficiencies $\eta_{h,i}$ and $\eta_{c,i}$ are required to calculate the resistance through the sides of the channels. These efficiencies are determined using the Eta_Fin_Straight_Rect function in EES, which assumes that the fin is straight with a rectangular base.

The resistance of the fins and the resistance of the fluid are in parallel, so an equivalent resistance $R_{eq,i}$ needs to be calculated for both hot and cold sides of the sub-HX. The total resistance is evaluated using these equivalent resistances.

$$\frac{1}{R_{eq,h,i}} = \left(\frac{1}{R_{conv,h,i}}\right)\left(N_{fin,h}+2\right) + \left(\frac{1}{R_{fin,h,i}}\right)\left(N_{fin,h}+1\right) \tag{2.51}$$

$$\frac{1}{R_{eq,c,i}} = \left(\frac{1}{R_{conv,c,i}}\right)\left(N_{fin,c}+2\right) + \left(\frac{1}{R_{fin,c,i}}\right)\left(N_{fin,c}+1\right) \tag{2.52}$$

$$R_{tot,i} = R_{eq,h,i} + R_{cond,i} + R_{eq,c,i} \tag{2.53}$$

The conductance UA_i, along with the total resistance $R_{tot,i}$, is used in Eq. (2.45) to solve for the length dx_i of each sub-HX. These sub-HX lengths are then added together to find the overall length of the recuperator.

$$Length = \sum_{i=1}^{N_{HX}} dx_i \tag{2.54}$$

2.6 Recuperator Effectiveness

The recuperator effectiveness is defined as the ratio of actual heat transferred to maximum heat transferred.

$$\varepsilon_{regen} = \frac{\dot{Q}_{regen}}{\dot{Q}_{max}} \tag{2.55}$$

The maximum heat transfer rate $\dot{Q}_{max}$ is evaluated by calculating the maximum heat transfer rate on both sides of the recuperator and taking the smaller of those two as the maximum.

$$\dot{Q}_{max,h} = \dot{m}\left(h_{\max,h,in} - h_{\max,h,out}\right) \tag{2.56}$$

$$\dot{Q}_{max,c} = \dot{m}\left(h_{\max,c,in} - h_{\max,c,out}\right) \tag{2.57}$$

The hot side maximum $\dot{Q}_{max,h}$ is defined as the mass flow rate times the difference in the maximum possible inlet and outlet specific enthalpies. These enthalpies are found based on the hot and cold inlet temperatures, $T_{h,in}$ and $T_{c,in}$, as well as the hot side pressure P_h. The cold side maximum $\dot{Q}_{max,c}$ is calculated in a similar manner, except that these enthalpies are evaluated at the cold side pressure P_c. In this case $\dot{Q}_{max}$ is equal to $\dot{Q}_{max,h}$.

2.7 Recuperator Mass

The mass of the recuperator m_{HX} is calculated by determining the average material density ρ_{HX} based on the average recuperator temperature. The volume of the heat exchanger material Vol_{HX} is calculated based on the dimensions of the recuperator.

$$Vol_{fin} = \left(t_h\right)\left(t_{fin}\right)\left(Length\right)\left(N_{fin}+2\right)\left(2\,N_{pair}\right) \tag{2.58}$$

$$\begin{aligned} Vol_{wall} = {} & \left(t_{wall}\right)\left(Width + t_{fin}\right)\left(Length\right)\left(N_{ch}+N_{fin}+1\right) \\ & + \left(t_{wall}\right)\left(t_{fin}\right)\left(Length\right)\left(N_{fin}+2\right) \end{aligned} \tag{2.59}$$

$$Vol_{HX} = Vol_{fin} + Vol_{wall} \tag{2.60}$$

$$m_{HX} = \rho_{HX}\ Vol_{HX} \tag{2.61}$$

The mass can also be determined based on porosity φ, which is calculated by dividing the volume of the channels Vol_{void} by the total volume of the recuperator Vol_{tot}.

$$Vol_{void} = \frac{N_{ch}}{2}\left(Width\right)\left(Length\right)\left(t_h + t_c\right) \tag{2.62}$$

$$Vol_{tot} = \left(Width_{HX}\right)\left(Length_{HX}\right)\left(Height_{HX}\right) \tag{2.63}$$

$$\varphi = \frac{Vol_{void}}{Vol_{tot}} \tag{2.64}$$

$$m_{HX} = \rho_{HX}\left(1-\varphi\right)Vol_{tot} \tag{2.65}$$

2.8 Stress Analysis

Because the recuperator is operating under such high pressures and temperatures, a stress analysis is especially important. This recuperator is designed for 3 times the pressure difference between the hot and cold channels to take into account large pressure differentials that might occur at startup and shutdown.

$$P_{design} = 3\left(P_{cold} - P_{hot}\right) \tag{2.66}$$

If a failure should occur within the recuperator, the bending stress on the plate could be large enough that the entire recuperator would unzip. To ensure that the recuperator can maintain its integrity despite such a failure, the channel wall is modeled as a beam with fixed ends.

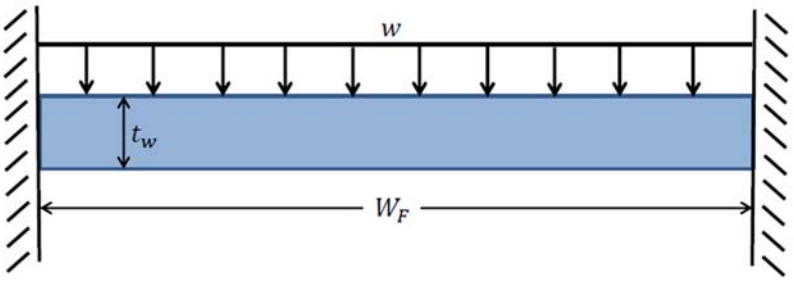

Figure 2.6: Diagram of the material between the hot and cold channels modeled as a beam with fixed ends under a uniform load.

In Figure 2.6, W_f refers to the length of the beam, which is twice the maximum width of the channel. This simulates a failure in which the passage width suddenly becomes twice as long as it should be. The load w placed on the beam is calculated based on the pressure difference between the hot and cold channels.

$$Force = P_{design}\ Area = P_{design}\left(W_f\right)\left(Length\right) \tag{2.67}$$

$$w = \frac{Force}{Length} = P_{design}\left(W_f\right) \tag{2.68}$$

The maximum shear and bending forces occur at the fixed ends of the beam in this situation. The shear and bending stresses that occur at these points, along with the respective factors of safety, are calculated using Eq. (2.69)−(2.74) (Juvinall et al., 2006).

$$M_{max} = -\frac{w\left(W_f\right)^2}{12} \tag{2.69}$$

$$V_{max} = \frac{wW_f}{2} \tag{2.70}$$

$$\sigma_{max} = \frac{M_{max}\,c}{I_p}\ where\ c = \frac{t_w}{2} \tag{2.71}$$

$$\tau_{max} = \left(\frac{3}{2}\right)\frac{V_{max}}{t_w\ Length} \tag{2.72}$$

$$FoS_{bend} = \frac{S_y}{\sigma_{max}} \tag{2.73}$$

$$FoS_{shear} = \frac{S_y}{\tau_{max}} \tag{2.74}$$

In Eq. (2.69) and (2.70), M_{max} and V_{max} represents the maximum bending moment and shear force, respectively. The variable σ_{max} refers to the bending stress in Eq. (2.71), and τ_{max} refers to the shear stress in Eq. (2.72). The bending factor of safety FoS_{bend} and shear factor of safety FoS_{shear} are calculated in Eq. (2.73) and (2.74) using the material's yield strength S_y

. Since the largest stresses are bending stresses, FoS_{bend} is set to 4 to meet ASME pressure vessel requirements. Equations (2.67)−(2.69), (2.71), and (2.73) can then be used to determine the maximum length of the beam, which in turn determines the maximum channel width that can be used.

3 Recuperator Modeling Results

The recuperator being investigated is meant to operate in a $10MW_e$ cycle. There are several sets of cycle conditions that generate $10MW_e$ of power. The cycle analyzed here assumes a compressor inlet temperature and pressure of 305 K and 10 MPa, and a turbine inlet temperature of 765 K and 25 MPa. The efficiency of the compressor is assumed to be 0.89, while the efficiency of the turbine is assumed to be 0.9 (Seidel, 2010). Once these conditions are set, the mass flow rate is modified until the net work output is 10 MW. The resulting cycle conditions are found in Table 3.1.

Table 3.1: Table of cycle conditions used in this investigation.

Cycle Conditions	
Compressor Inlet Temperature [K]	305
Compressor Inlet Pressure [MPa]	10
Turbine Inlet Temperature [K]	765
Turbine Inlet Pressure [MPa]	25
Mass Flow Rate [kg/s]	111.3
Compressor Efficiency	0.89
Turbine Efficiency	0.9
Net Work [MW]	10

3.1 Model Convergence

As mentioned in Section 2.2, the recuperator is modeled using several sub-HXs. If there are too few sub-heat exchangers, the effect of property variations in the supercritical CO_2 is not captured correctly. Too many sub-heat exchangers, however, would result in a long computation time. To find the right number, the recuperator is first modeled with 200 sub-HXs and the result is taken as the "correct" length, as shown in Figure 3.1. The number of sub-HXs is then varied between 1 and 200, and the percent difference between the modeled length and the correct length is found using Eq. (3.1).

$$Percent\ Difference = 100\left(\frac{Length - Length_{act}}{Length_{act}}\right) \tag{3.1}$$

This percent difference can be seen in Figure 3.1.

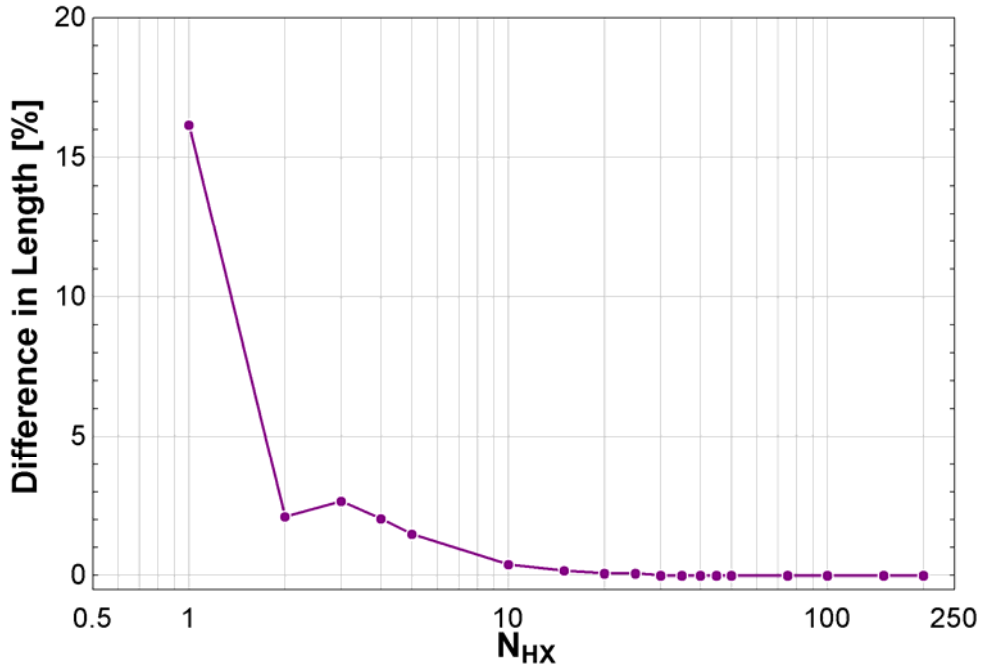

Figure 3.1: Plots of percent difference in length versus number of sub heat-exchangers.

At least 20 sub-HXs are needed to achieve a variation of 0.1% or less in the length. Since there is not much difference in computation time between 20 and 25 sub-HXs, 25 sub-HXs are used for all future calculations.

3.2 Model Confirmation

Before any optimization takes place, a PCHE currently being used by Sandia National Laboratories (Sandia) is simulated to confirm the results of the model. In conjunction with the U.S. Department of Energy Office of Nuclear Energy (DOE-NE), Sandia has developed an S-CO_2 Brayton cycle Test Assembly to explore potential technical issues and confirm

estimates of system performance. An assembly schematic can be found in Figure 3.2 (Sandia 2012):

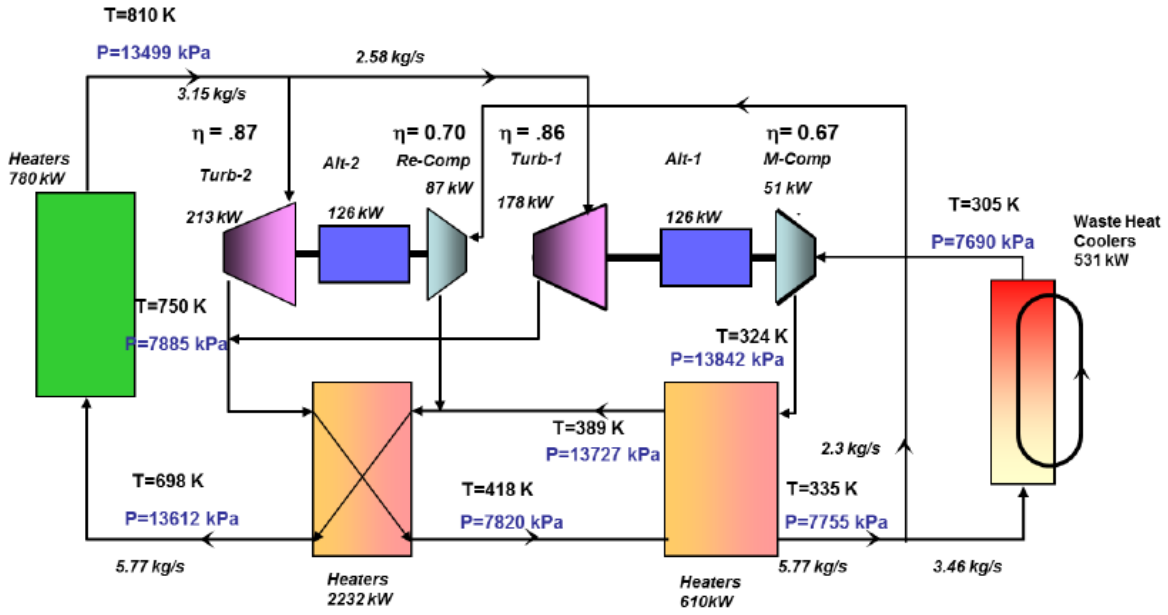

Figure 3.2: Schematic of Sandia's split flow recompression test cycle. The HT recuperator is on the left.

The current assembly is a split flow setup, with two PCHEs acting as high temperature (HT) and low temperature (LT) recuperators. The HT recuperator is the one that will be simulated using the PCHE model. It is designed to transfer 2.3 MW at a flow rate of 5.7 kg/s, with a hot-side inlet temperature of 755 K and a maximum allowable working pressure of 17.2 MPa. The approximate dimensions of this recuperator can be found in Table 3.2.

Table 3.2: Table of dimensions for Sandia's high temperature recuperator (Sandia 2012).

Property	Value
HT Recuperator	
Channel Width	1.27 mm (0.05 in.)
Channel Depth	0.77mm (0.0303 in.)
Plate Depth	1.69 mm (0.0665 in.)
Flow Area per Channel	0.768 mm^2 (0.00119 $in.^2$)
Hydraulic Diameter (Dh)	1.0607 mm (0.0418 in.)
Core	
Height	0.296 m (11.65 in.)
Length	0.996 m (39.21 in.)
Width	0.512 m (20.16 in.)
Heat Transfer Area	43 m^2 (462.80 ft^2)
Core Mass	1410 kg (3108 lbm)

To model this recuperator, the channel width, the channel depth t_h and t_c, and the overall width and height are set using the dimensions given. EES then solves for the overall length that produces the heat transfer rate and adjust the number of channels to produce the pressure drops found in Figure 3.2. The results can be found in Table 3.3.

Table 3.3: Results of Sandia model.

HT Recuperator (Model)		
Channel Width	1.27	mm
Channel Depth	0.77	mm
Plate Depth	1.69	mm
Height	0.296	m
Width	0.512	m
Length	1.214	m
Mass	1302	kg
Q_regen	2.232	MW
dP_HTCB	66	kPa
dP_CTHB	116	kPa

The length produced by the model differs from the actual recuperator length by 20%, and the mass differs by 8%. This is because the model assumes that the channels are straight and rectangular, but the type of channels used in Sandia's PCHE is unknown. Non-straight channels, such as zigzag or sinusoidal geometries, could account for this discrepancy, which suggests that this model is a reasonable approximation of the HT recuperator.

3.3 Model Optimization

The optimized recuperator is designed for a 0.5% pressure drop relative to the inlet pressure on both the hot and cold sides of the channel, which ultimately sets both the channel geometry and the number of channels on each side. To mimic the dimensions of Sandia's HT recuperator, the wall thickness t_{wall} and hot side fin thickness $t_{fin,h}$ are each set to 1 mm, and the channel width is set to be twice as large as the channel height. If this value is larger than the maximum width calculated in Section 2.8, then the channel width is adjusted to the maximum limit.

The overall width and height of the heat exchanger are set to be equal, so that the frontal cross-section of the recuperator is square. The frontal area is then varied between 0.64 and 4.0 m^2 (Figure 3.3).

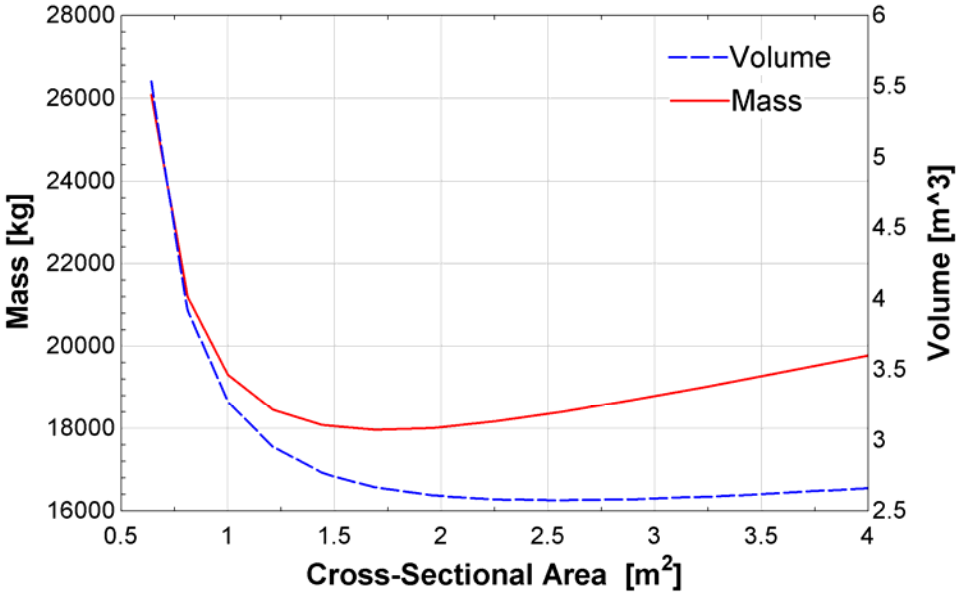

Figure 3.3: Plot of recuperator mass and volume versus cross sectional area.

Figure 3.3 shows that there is a minimum volume of 3.0 m^3 that occurs around an area of 2.56 m^2. The minimum mass of 18,000 kg occurs at an area of 1.69 m^2. This is because at smaller areas, the change in void volume is what dominates the change in total volume. But around an area of 2.56 m^2 the void volume is small enough that it no longer has a significant effect on the total volume, and instead the change in material volume dominates (Figure 3.4). It is the interaction between these two variables that causes the fluctuation in mass in Figure 3.3.

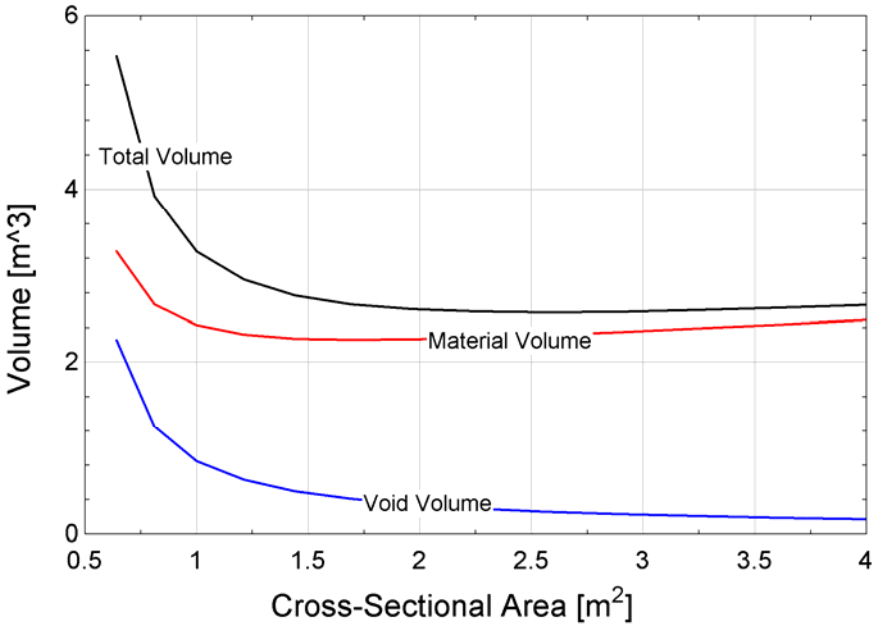

Figure 3.4: Plot of void, material, and total volume vs recuperator width.

The recuperator with the smallest total volume is used to match the performance of the regenerator in Chapters 4 and 5. The characteristics of this recuperator can be found in Table 3.4.

Table 3.4: Results for optimized recuperator model.

Optimized Operating Conditions	
Cycle Power [MW_e]	10.0
Thermal Power [MW_{th}]	46.1
Hot Side Pressure Drop [kPa]	50
Cold Side Pressure Drop [kPa]	125
Hot Side Reynolds Number	14145
Cold Side Reynolds Number	28378
Total Volume [m^3]	2.58
Heat Transfer Area [m^2]	1686
Mass [kg]	18404
Overall Width [m]	1.60
Overall Height [m]	1.60
Overall Length [m]	1.00
Channel Height [mm]	0.47
Channel Width [mm]	0.93
Fin Thickness [mm]	1.00
Wall Thickness [mm]	1.00

4 Regenerator Modeling Methods

4.1 Assumptions

The flow and heat transfer of S-CO_2 within a regenerator is transient due to the switching of the hot and cold streams between two tanks, though it may eventually reach a periodic steady state in which the properties of the fluid and the regenerator periodically return to their values at the start of a cycle. This means that energy storage in the both the regenerator material and fluid need to be taken into account. Since the working fluid is supercritical it cannot be treated as an ideal gas, and its properties cannot be assumed constant (see Figure 1.3). Secondary effects such as pressure drop, axial conduction, and conduction within the spheres in the packed bed are all present in the actual process. In this study, the regenerator is assumed to be composed of a bed of packed spheres and is assumed to experience balanced, asymmetric flow, which means that the mass flow rate is the same for both the hot-to-cold blow and the cold-to-hot blow, but the heat transfer coefficient is not the same.

Initially, it is assumed that there is no axial conduction along the regenerator and no temperature gradient within the spheres. It is also assumed that there is no pressure drop and negligible entrained fluid heat capacity. Once the model has been successfully created using these assumptions, these effects will be considered approximately as secondary loss mechanisms.

4.2 Governing Equations

The temperature distribution within the regenerator is modeled by solving a set of partial, differential equations that are obtained from energy balances on the fluid and the matrix. The derivation of these equations is described in the following sections.

4.2.1 Governing Equations for the Working Fluid

A differential segment of fluid is illustrated in Figure 4.1.

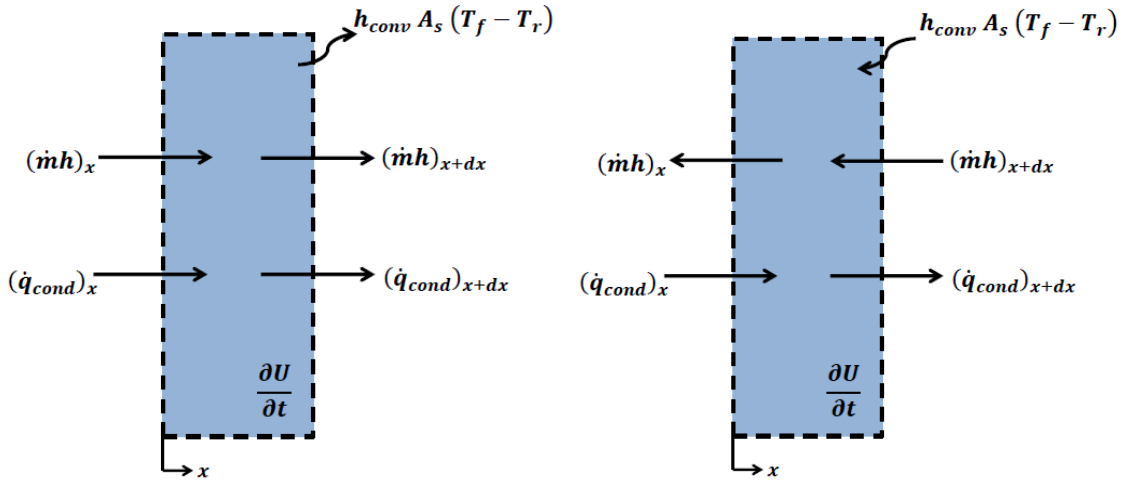

Figure 4.1: Energy balance on a differential segment of fluid for (a) the hot-to-cold blow (b) the cold-to-hot blow.

In Figure 4.1, $\dot{q}_{cond}$ represents the conductive heat transfer rate through the fluid, and $\frac{\partial U}{\partial t}$ represents the energy stored by the entrained fluid. The amount of energy transferred across the control volume by the movement of fluid is represented by the product of the mass flow rate $\dot{m}$ and the fluid enthalpy h. Since axial conduction and entrained fluid heat capacity are neglected, these energy balances simplify to Eq. (4.1) and (4.2)

$$0 = \dot{m}\frac{\partial h}{\partial x}dx + h_{conv}\,A_s\left(T_f - T_r\right) for\, 0 < t < t_b \tag{4.1}$$

$$\dot{m}\frac{\partial h}{\partial x}dx = h_{conv}\,A_s\left(T_f - T_r\right) for\, t_b < t < 2t_b \tag{4.2}$$

In these equations, t_b represents the time for one blow process. The hot-to-cold blow occurs while $0 < t < t_b$, and the cold-to-hot blow occurs while $t_b < t < 2t_b$. The mass flow rate of the

fluid can be calculated as the product of the density of the fluid, ρ_f, the cross sectional area of the fluid $A_{c,fluid}$, and the velocity of the fluid *vel*.

$$\dot{m} = \rho_f \, vel \, A_{c,fluid} \tag{4.3}$$

The cross sectional area for the fluid is defined as

$$A_{c,\,fluid} = \varphi \, A_c \tag{4.4}$$

where φ represents the porosity of the packed bed. The convection surface area, A_s, can be calculated using Eq. (4.5).

$$A_s = \alpha_s \, A_c \, \Delta x \tag{4.5}$$

In this equation Δx represents the length of the differential segment, and α_s represents the specific surface area of the fluid, which is the surface area of the packing material per unit volume. This surface area depends on the type of matrix used; for a bed of packed spheres, it can be calculated using the porosity of the bed and the diameter of the spherical particles d_p (Nellis 2009):

$$\alpha_s = \frac{6(1-\varphi)}{d_p} \tag{4.6}$$

By using Eq. (4.3)−(4.6) the energy equations defined in Eq. (4.1) and (4.2) can be represented as

$$0 = \rho_f \, vel \, \varphi \frac{\partial h}{\partial x} + h_{conv} \, \alpha_s \left(T_f - T_r\right) for \, 0 < t < t_b \tag{4.7}$$

$$\rho_f \, vel \, \varphi \frac{\partial h}{\partial x} = h_{conv} \, \alpha_s \left(T_f - T_r\right) for \, t_b < t < 2t_b \tag{4.8}$$

The spatial rate of change in enthalpy $\frac{\partial h}{\partial x}$ can be rewritten in terms of $\frac{\partial T}{\partial x}$ and $\frac{\partial P}{\partial x}$ using the multivariable chain rule.

$$\frac{\partial h}{\partial x} = \left(\frac{\partial h}{\partial T}\right)_P \frac{\partial T_f}{\partial x} + \left(\frac{\partial h}{\partial P}\right)_T \frac{\partial P}{\partial x} \tag{4.9}$$

The specific heat capacity at constant pressure is defined as

$$c_P = \left(\frac{\partial h}{\partial T}\right)_P \tag{4.10}$$

Since pressure drop is neglected across the regenerator, Eq. (4.9) simplifies to

$$\frac{\partial h}{\partial x} = c_P \frac{\partial T_f}{\partial x} \tag{4.11}$$

This definition is then substituted into Eq. (4.7) and Eq. (4.8) to produce Eq. (4.12) and (4.13).

$$0 = \rho_f \; vel \; \varphi \; c_P \frac{\partial T_f}{\partial x} + \; h_{conv} \; \alpha_s \left(T_f - T_r\right) for 0 < t < t_b \tag{4.12}$$

$$\rho_f \; vel \; \varphi \; c_P \frac{\partial T_f}{\partial x} = \; h_{conv} \; \alpha_s \left(T_f - T_r\right) for \; t_b < t < 2 \; t_b \tag{4.13}$$

These equations represent the final fluid energy equations used to investigate the performance of the regenerator.

4.2.2 Governing Equations for Regenerator Material

A similar process can be used to derive the equation used for the regenerator material. A differential segment of material is illustrated in Figure 4.2.

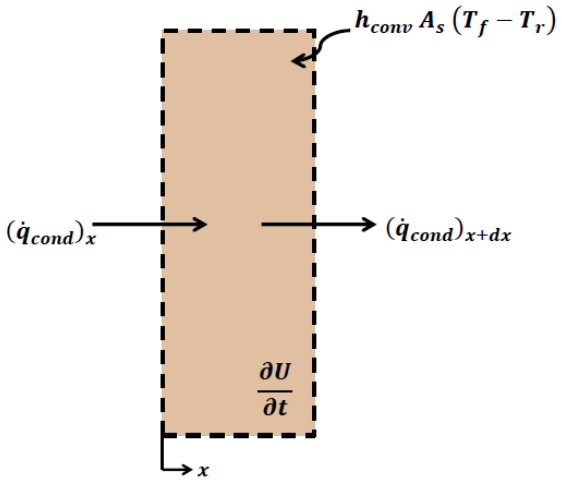

Figure 4.2: Energy balance on a differential segment of material. The energy balance is the same for both the hot-to-cold blow and the cold-to-hot blow.

As with the fluid, the conduction through the material is neglected in this model. Therefore, the energy balance for the material can be written as

$$m_r \frac{\partial u_r}{\partial t} = h_{conv}\, A_s \left(T_f - T_r\right) for 0 < t < 2\, t_b \tag{4.14}$$

This equation is the same for both the hot-to-cold blow and the cold-to-hot blow. The mass of the material is defined as

$$m_r = \rho_r\, Vol_r = \rho_r \left(1-\varphi\right)\, A_c\, dx \tag{4.15}$$

where ρ_r is the density of the material and Vol_r is the material volume.

The change in internal energy of the regenerator material, $\frac{\partial u_r}{\partial t}$ can be written in terms of the change in temperature and specific volume using the chain rule.

$$\frac{\partial u_r}{\partial t} = \left(\frac{\partial u_r}{\partial T}\right)_v \frac{\partial T_r}{\partial t} + \left(\frac{\partial u_r}{\partial v}\right)_T \frac{\partial v}{\partial t} \tag{4.16}$$

The specific heat capacity at constant volume is defined as

$$c_r = \left(\frac{\partial u_r}{\partial T} \right)_v \frac{\partial T_r}{\partial t} \tag{4.17}$$

This definition is used to simplify Eq. (4.16). Since the material is incompressible, its volume is not changing with time. Therefore, the change in internal energy over time can be rewritten as

$$\frac{du_r}{dt} = c_r \frac{dT_r}{dt} \tag{4.18}$$

The definition for A_s is the same as in Eq. (4.5). Substituting Eq. (4.15) and (4.18) into Eq. (4.14) produces the energy balance for the regenerator material.

$$\rho_r \left(1-\varphi\right) c_r \frac{dT_r}{dt} = h_{conv} \alpha_s \left(T_f - T_r\right) for 0 < t < 2\ t_b \tag{4.19}$$

4.3 Numerical Method

The energy equations derived in the previous section (Eq. (4.12), (4.13), and (4.19)) can be used to create a system of equations that will predict the fluid and material temperatures over one cycle. In order to solve this system of equations, both the length of the regenerator and the time associated with one cycle are discretized. An illustration of this discretization can be found in Figure 4.3.

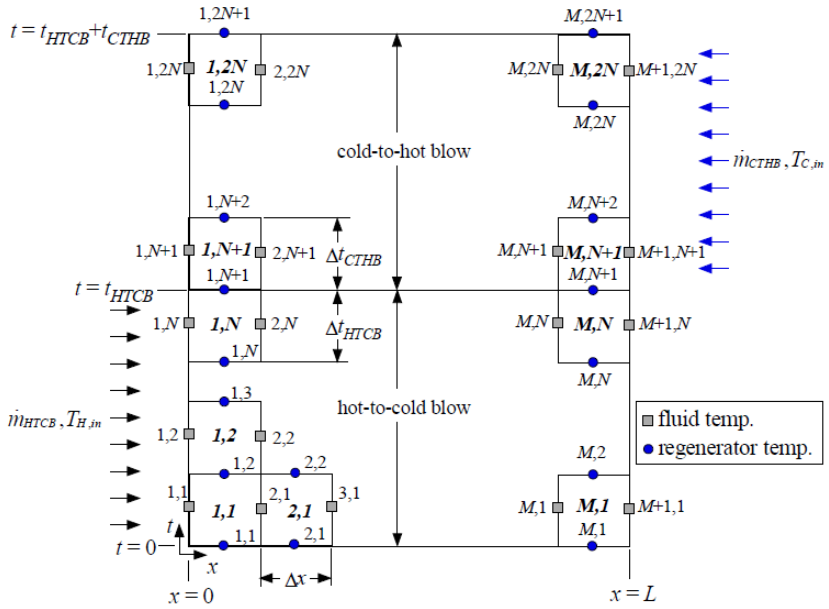

Figure 4.3: Regenerator discretized in space and time

The variable *M* represents the total number of discretized sections through space, and *N* represents the total number of sections through time; this model uses 100 nodes for each.. A single discretized section for the hot-to-cold blow and cold-to-hot blow is shown in Figure 4.4.

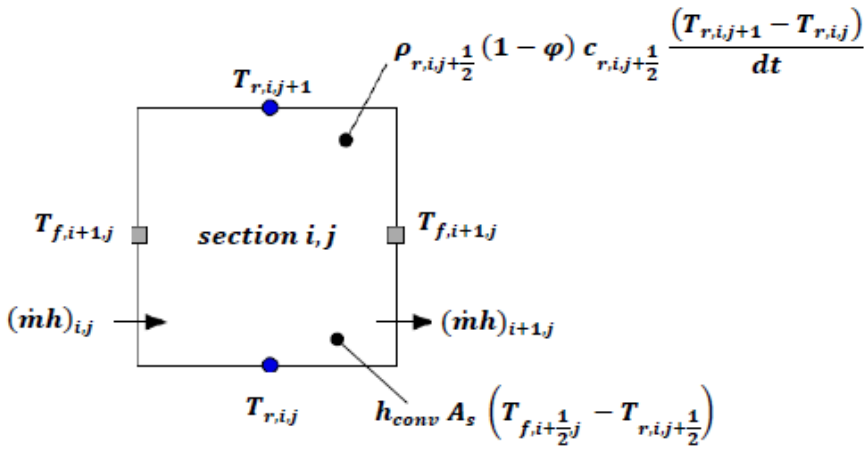

(a)

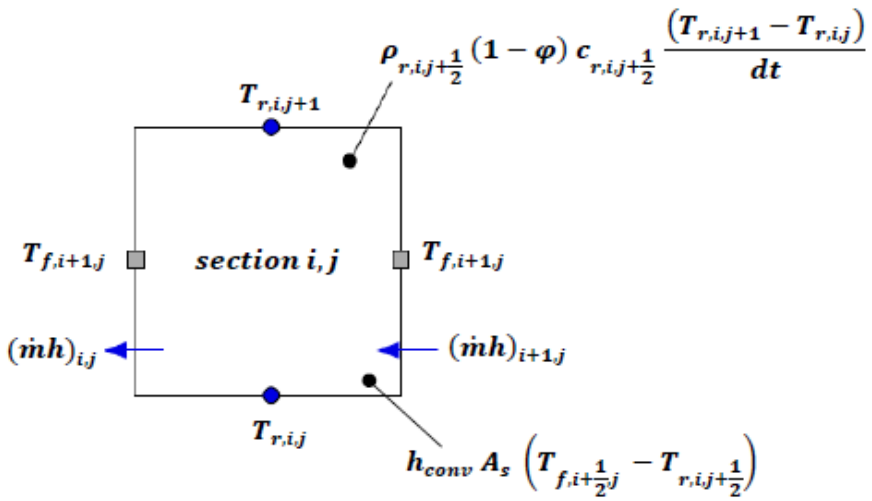

(b)

Figure 4.4: Energy balance for section i,j during (a) the hot-to-cold blow and (b) the cold-to-hot blow.

Using the energy equations derived in the previous sections, Eq. (4.12) can be rewritten as

$$\left(\rho_f\ vel\right) c_{P\,i+\frac{1}{2},j}\ \varphi\frac{\left(T_{f\,i+1,j}-T_{f\,i,j}\right)}{dx}\ +h_{conv\,i+\frac{1}{2},j}\ \alpha_s\left(T_{f\,i+\frac{1}{2},j}-T_{r\,i,j+\frac{1}{2}}\right)=0 \tag{4.20}$$

for i=1:M and j=1:N

The fluid properties must be averaged to find the properties at the center of the discretized section, as indicated in Eq. (4.21) and Eq. (4.22). Likewise, the fluid and regenerator temperatures must be averaged in order to accurately calculate the heat transferred via convection (Eq. (4.23))

$$c_{P\,i+\frac{1}{2},j}=\frac{1}{2}\left[c_{P\,i,j}+c_{P\,i+1,j}\right] \tag{4.21}$$

$$h_{conv\,i+\frac{1}{2},j}=\frac{1}{2}\left[h_{conv\,i,j}+h_{conv\,i+1,j}\right] \tag{4.22}$$

$$\left(T_{f\,i+\frac{1}{2},j}-T_{r\,i,j+\frac{1}{2}}\right)=\frac{1}{2}\left[T_{f\,i,j}+T_{f\,i+1,j}-T_{r\,i,j}-T_{r\,i,j+1}\right] \tag{4.23}$$

For all of these equations, coordinate *i* represents the current point in space, and coordinate *j* represents the current point in time. Eq. (4.13) and (4.19) are discretized in a similar manner:

$$\left(\rho_f \ vel\right) c_{P\, i+\frac{1}{2},j} \ \varphi \frac{d\left(T_{f\, i+1,j} - T_{f\, i,j}\right)}{dx} = h_{conv\, i+\frac{1}{2},j} \ \alpha_s \left(T_{f\, i+\frac{1}{2},j} - T_{r\, i,j+\frac{1}{2}} \right) \tag{4.24}$$

for i=1:M and j=N+1:2N

$$\left(\rho_r \ c_r\right)_{i+\frac{1}{2},j} \left(1-\varphi\right) \frac{d\left(T_{r\, i,j+1} - T_{r\, i,j}\right)}{dt} = h_{conv\, i+\frac{1}{2},j} \ \alpha_s \left(T_{f\, i+\frac{1}{2},j} - T_{r\, i,j+\frac{1}{2}} \right) \tag{4.25}$$

for i=1:M and j=1:2N

The inlet conditions for the fluid are known for both the hot-to-cold blow and the cold-to-hot-blow, and the material temperature at the end of one blow must equal the temperatures at the beginning of the next blow during operation at periodic steady state. These boundary conditions can be written in discretized form as follows:

$$T_{f1,j} = T_{H,in} \quad for\, j = 1:N \tag{4.26}$$

$$T_{f\, M+1,j} = T_{C,in} \quad for\, j = N+1:2N \tag{4.27}$$

$$T_{r\, i,1} = T_{r\, i,2N+1} \quad for\, j = 1:2N+1 \tag{4.28}$$

4.4 Regenerator Effectiveness

The regenerator effectiveness is determined using Eq. (4.29).

$$\varepsilon_{regen} = \frac{Q_{fluid}}{Q_{max}} \tag{4.29}$$

The heat transfer through the regenerator is found using Eq. (4.30) below.

$$Q_{fluid} = \sum_{i=1}^{M} \sum_{j=1}^{N} \varphi A_c \left(\rho_f vel\right)_{i,j} c_{P,i+\frac{1}{2},j} \left(T_{f,i+1,j} - T_{f,i,j}\right) dt \tag{4.30}$$

The maximum heat transfer Q_{max} is evaluated by calculating the maximum heat transfer during both the hot-to-cold blow and the cold-to-hot blow. The minimum of these two is used as Q_{max}

$$Q_{max,HTCB} = \dot{m}\left(h_{\max,h,in} - h_{\max,h,out}\right) t_b \tag{4.31}$$

$$Q_{max,CTHB} = \dot{m}\left(h_{\max,c,in} - h_{\max,c,out}\right)t_b \tag{4.32}$$

The hot-to-cold blow maximum $Q_{max,HTCB}$ is defined as the mass flow rate times the cycle time t_b and the difference in the maximum possible inlet and outlet specific enthalpies. These enthalpies are found based on the hot and cold inlet temperatures, $T_{h,in}$ and $T_{c,in}$, as well as the hot side pressure P_h. The cold-to-hot blow maximum $Q_{max,CTHB}$ is calculated in a similar manner, except that these enthalpies are evaluated at the cold side pressure P_c.

4.5 Fluid Properties

The properties of carbon dioxide are obtained from Northland Numeric's FIT library (Northland Numerics, 2014), which uses an interpolation-based approach that has been verified using REFPROP (National Institute of Standards and Technology, 2014).

The Reynolds number Re_f for a packed bed of spheres is calculated based on the density ρ_f, viscosity $\boldsymbol{\mu_f}$, and velocity of the fluid, as well as the average sphere diameter.

$$Re_f = \frac{\rho_f \; d_p \; vel}{\mu_f} \tag{4.33}$$

This dimensionless parameter, along with the Prandtl number Pr_f, is used to calculate the Nusselt number Nu_f using Rohsenow's correlation for a bed of packed spheres (Rohsenow 1998).

$$Nu_f = 2 + 1.8 \; Re_f^{1/2} \; Pr_f^{1/2} \tag{4.34}$$

where the Prandtl number is defined as

$$Pr_f = \frac{c_f \, \mu_f}{k_f} \tag{4.35}$$

4.6 Model Algorithm

If the set of equations derived in Sections 4.2 and 4.3 were linear, they could be solved using a single matrix inversion in MATLAB. However, the properties of carbon dioxide can vary significantly within the supercritical region, which makes these equations nonlinear. Successive substitution is used to solve this nonlinear system of equations, as indicated in Figure 4.5.

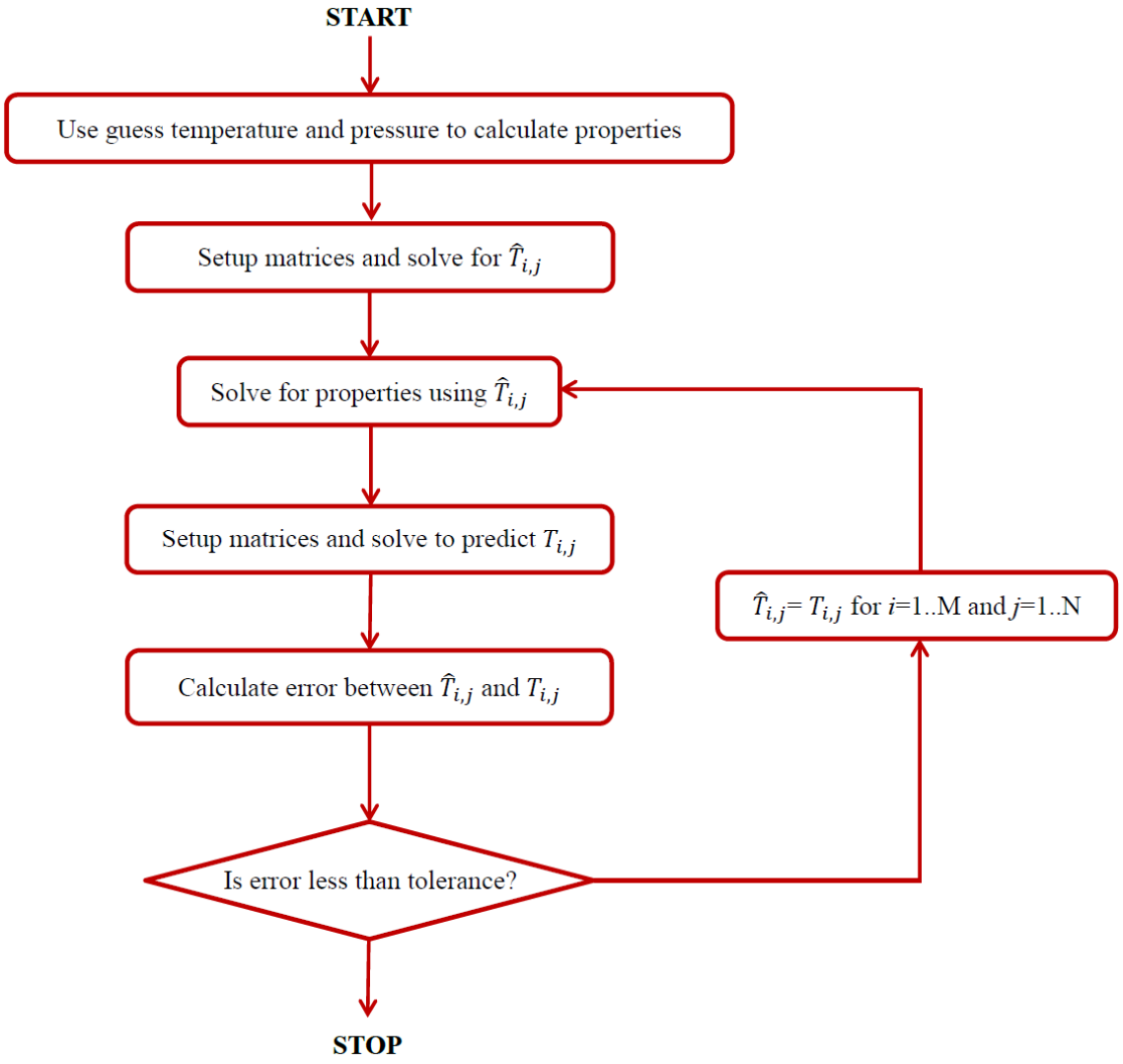

Figure 4.5: Flow chart for regenerator code.

Initially, the properties are calculated using a set of guess temperatures. These properties are then used to solve the discretized energy equations. The resulting temperature matrix $\hat{\boldsymbol{T}}_{\boldsymbol{i,j}}$ is then used to update the properties of the fluid, and a new temperature distribution $\boldsymbol{T}_{\boldsymbol{i,j}}$ is calculated in the same manner as before. The error between these two distributions is defined below.

$$err_{i,j} = \sqrt{\frac{\left(\hat{T}_{i,j} - T_{i,j}\right)^2}{(2N+1)M}} \tag{4.36}$$

If the minimum error between $\hat{T}_{i,j}$ and $T_{i,j}$ is above the specified tolerance, which set to 0.01, then $\hat{T}_{i,j}$ is updated for the next iteration. This cycle continues until the error is below the tolerance.

4.7 Vectorized Model

Typically, programming languages utilize FOR loops to build matrices and arrays. But since MATLAB is an array-based language, building matrices all at once with the SPARSE command allows for faster calculations. A simplified example of each code can be found below.

```
% SIMPLE FOUR LOOP
% --------------------------------
clear mem
A=spalloc(M,N,M*4);

    for i=1:M
      for j=1:N
         A((j-1)*M+i,(j-1)*M+i)=1;
         A((j-1)*M+i,(j+1-1)*M+i)=2;
         A((j-1)*M+i,(2*N+1)*M+(j-1)*(M+1)+i)=3;
         A((j-1)*M+i,(2*N+1)*M+(j-1)*(M+1)+i+1)=4;
      end
    end
```

```
% SIMPLE VECTORIZED MATRIX
% --------------------------------
clear mem
A=spalloc(M,N,M*4);

i=repmat(1:M,N-1,1);
j=sortrows(repmat(1:N,M-1,1));
A=A+sparse((j-1)*M+i,(j-1)*M+i,1,M,N);
A=A+sparse((j-1)*M+i,(j+1-1)*M+i,2,M,N);
A=A+sparse((j-1)*M+i,(2*N+1)*M+(j-1)*(M+1)+i,3,M,N);
A=A+sparse((j-1)*M+i,(2*N+1)*M+(j-1)*(M+1)+i+1,4,M,N);
```

In each of these codes, memory is allocated to the sparse matrix using the SPALLOC command. The inputs for this command are the number of rows, number of columns, and

number of non-zero elements in the matrix, respectively. In the first code, matrix A is built using a double for loop. But in the second code, matrix A is built using the SPARSE command. First, an array *i* of row coordinates and an array *j* of column coordinates are created using the REPMAT and SORTROWS commands. These coordinates are then used to define the location of each nonzero element in the matrix. When using the SPARSE command, the first two inputs are the desired row and column, respectively. The third input is the value at that element in the matrix, and the final two inputs represent the size of the matrix. This simple code was used to compare the computation time of matrix A for various grid sizes (Figure 4.6).

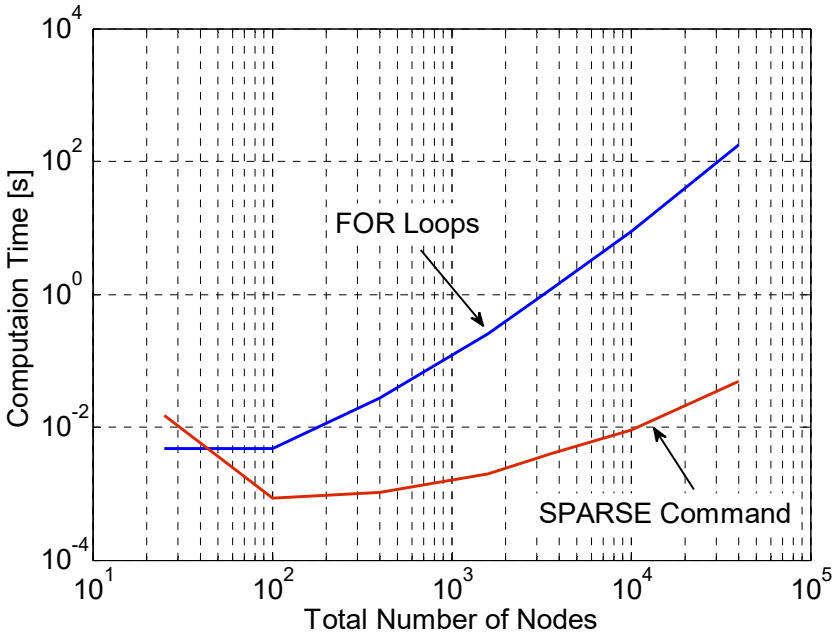

Figure 4.6: Computation time vs number of nodes

There is not much difference in computation time at small grid sizes. In fact, when the grid is small enough, FOR loops are faster. But as the total number of nodes increases, the computation time associated with FOR loops rises much more quickly; at 40,000 nodes it takes about 3 minutes to build a matrix with FOR loops, and it only take 0.05 seconds with

the SPARSE command. Since the regenerator model needs a large number of nodes to accurately capture the changes in temperature, the SPARSE command is used to keep computation time at a minimum.

4.8 Model Verification

The results from the regenerator model can be verified by comparing them to the exact solution derived by Dragutinovic and Baclic (1998). Their analytical solution was used to create a series of tables for the effectiveness of a regenerator based on several dimensionless parameters. These dimensionless parameters are defined in Eq. (4.37)–(4.41).

$$\Lambda = \frac{h_{conv}\ A_s}{\dot{m}\ c_f} = NTU \tag{4.37}$$

$$\Pi = \frac{h_{conv}\ A_s\ t_b}{m_r\ c_r} = \frac{h_{conv}\ \alpha\ t_b}{(1-\theta)\ \rho_r\ c_r} \tag{4.38}$$

$$U = \frac{\dot{m}\ c_f\ t_b}{(1-\theta)\ \rho_r\ c_r} = \frac{\Pi}{\Lambda} \tag{4.39}$$

$$\beta = \frac{U_1}{U_2} \tag{4.40}$$

$$\sigma = \frac{\Lambda_1}{\Lambda_2} \tag{4.41}$$

The variable Λ is referred to as a reduced length, and has the same definition as NTU. Both the reduced length and the reduced time Π are used to find the utilization factor U, which in turn is used to calculate the unbalance factor β of the regenerator. Reduced length is also used to calculate the asymmetry factor σ. In Eq. (4.38) and (4.39), subscript 1 refers to the hot-to-cold blow, and subscript 2 refers to the cold-to-hot blow.

Carbon dioxide was used in the numerical model with constant properties to obtain results that can be compared with those in Dragutinovic and Baclic (1998). The blow time and the geometry were then altered to produce different balance and asymmetry factors. In Figure 4.7, the circles represent the numerical results, and the lines represent the exact solution.

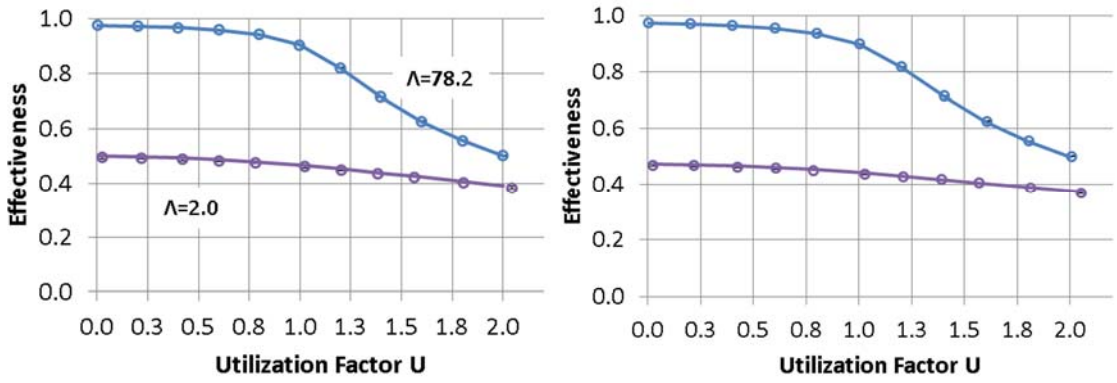

Figure 4.7: Comparison between numerical and published results for (a) balanced, symmetric flow (β=1, σ=1), and (b) balanced, asymmetric flow (β=1, σ=0.8).

Figure 4.7 shows that the numerical results match within 0.1% of the published results, which means that this model produces an accurate representation of the regenerator's performance.

4.9 Model Complexities

Once the simple model has been verified, additional effects are considered and approximately added in order to create a more realistic simulation.

4.9.1 Temperature Gradient within Spheres

The temperature through a sphere is not necessarily uniform, especially if the conductivity of a material is low. To determine if the thermal resistance within a solid material can be ignored, the Biot number is calculated using the conductivity of the material, the radius of the

spheres in the packed bed, and the heat transfer coefficient between the fluid and the material.

$$Bi = \frac{r_{dp}\, h_{conv}}{k_r} \tag{4.42}$$

This number is then used to calculate an effective convection coefficient h_{eff} using Eq. (4.43). This equation was derived by Handley and Heggs in 1968 as a means of approximating the effects of internal sphere conductivity.

$$h_{eff} = \frac{h_{conv}}{1 + \frac{Bi}{5}} \tag{4.43}$$

If the Biot number is less than 0.1, then the conductive resistance within the spheres is small compared to the convective resistance at the surface, and the effective coefficient approaches h_{conv}. The variable h_{eff} is substituted into the model to account for temperature gradients within the spheres.

4.9.2 Entrained Fluid and Axial Conduction

In Section 4.2, Eq. (4.12) and (4.13) show that the energy transferred to and from the packed bed via conduction Q_{conv} is equal to the energy in the fluid Q_{fluid}. Both of these equations neglect the energy conducted along the length of the regenerator Q_{axial} and the energy stored in the entrained fluid Q_{stored}. These terms are taken into account by subtracting them from the energy in the fluid.

$$Q_{fluid,eff,HTCB} = Q_{fluid} - Q_{axial,HTCB} - Q_{stored,HTCB} \tag{4.44}$$

$$Q_{fluid,eff,CTHB} = Q_{fluid} - Q_{axial,CTHB} - Q_{stored,CTHB} \tag{4.45}$$

Eq. (4.44) is used to calculate the effective heat transferred for the hot-to-cold blow, and Eq. (4.45) is used for the cold-to-hot blow. The effectiveness is then calculated using the minimum $Q_{fluid,eff}$.

The equations for energy stored in the entrained fluid is found in Eq. (4.46) and Eq. (4.47). The variable c_v refers to the specific heat of the fluid at constant volume.

$$Q_{stored,HTCB} = \sum_{i=1}^{M}\sum_{j=1}^{N} \varphi\, A_c\, dx \left(\rho_f c_v\right)_{i+\frac{1}{2},j} \left(T_{f,i+\frac{1}{2},j+1} - T_{f,i+\frac{1}{2},j} \right) \tag{4.46}$$

$$Q_{stored,CTHB} = \sum_{i=1}^{M}\sum_{j=N+1}^{2N} \varphi\, A_c\, dx \left(\rho_f c_v\right)_{i+\frac{1}{2},j} \left(T_{f,i+\frac{1}{2},j+1} - T_{f,i+\frac{1}{2},j} \right) \tag{4.47}$$

The equations for axial conduction are written as follows:

$$Q_{axial,HTCB} = -\varphi\, A_c\, k_{eff,avg,HTCB} \frac{\left(T_{f,M+1,1} - T_{f,1,1}\right)}{L} dt \tag{4.48}$$

$$Q_{axial,CTHB} = -\varphi\, A_c\, k_{eff,avg,CTHB} \frac{\left(T_{f,M+1,N+1} - T_{f,1,N+1}\right)}{L} dt \tag{4.49}$$

The variable L refers to the total length of the regenerator. In Eq. (4.48) and (4.49), $k_{eff,avg,HTCB}$ and $k_{eff,avg,CTHB}$ are the average effective conductivities for the hot-to-cold blow and the cold-to-hot blow, respectively. The effective conductivity k_{eff} accounts for both static conduction k_{static} and dispersion D_d within the regenerator.

$$k_{eff} = k_{static} + D_d \tag{4.50}$$

The variable k_{static} is found using a correlation that modifies the Maxwell model to predict static conductivity for materials with a medium-dense porosity ($\varphi = 0.15 to 0.85$, Gonzo 2002). The Maxwell model is defined in Eq. (4.51).

$$\frac{k_{static}}{k_f} = \frac{1+2\beta(1-\varphi)}{1-\beta(1-\varphi)} \tag{4.51}$$

where

$$\beta = \frac{k_r - k_f}{k_r + 2k_f} \tag{4.52}$$

According to Gonzo, this model predicts the static thermal conductivity of high porosity materials ($\varphi > 0.85$) very well, but it is less accurate at lower porosities. Gonzo's adjusted correlation for medium-dense materials can be found in Eq. (4.53).

$$\frac{k_{static}}{k_f} = \frac{1+2\beta(1-\varphi)+\left(2\beta^3-0.1\beta\right)(1-\varphi)^2+(1-\varphi)^3\ 0.05\ e^{4.5\beta}}{\left(1-\beta(1-\varphi)\right)} \tag{4.53}$$

A plot of k_{static} at various porosities can be found in Figure 4.8.

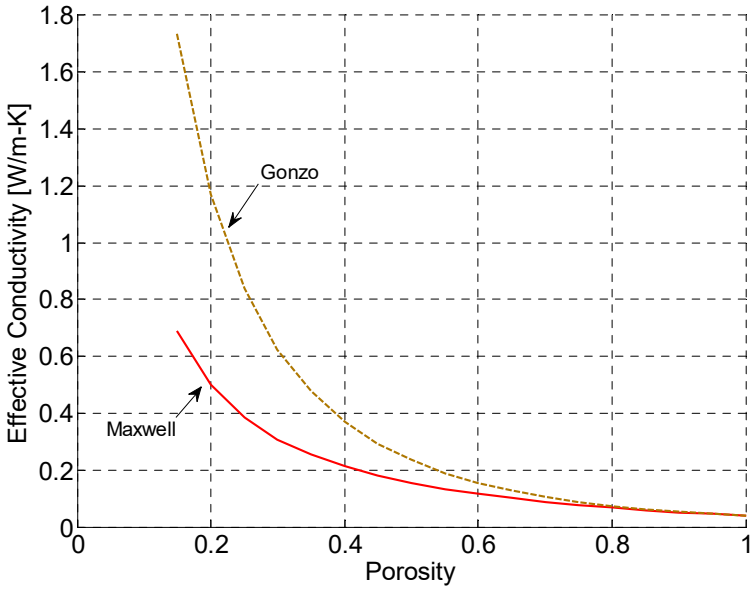

Figure 4.8: Comparison of static conductivity models for both high and medium porosity materials.

The conductivities used in this comparison correspond to the average operating conditions within the regenerator. Figure 4.8 shows that Gonzo's and Maxwell's correlations are in

agreement at porosities greater than 80%. As the porosity decreases, these correlations diverge significantly. Gonzo used Eq. (4.52) and (4.53) to estimate the effective conductivity to within 10% of published experimental results, so his correlation will be used in this model.

The dispersion term in Eq. (4.50) is calculated using the correlation below (Vafai 2000).

$$D_d = 0.1\left(Pe\right)\ k_f = 0.1\left(Re\right)\left(Pr\right)k_f \tag{4.54}$$

According to Vafai, this correlation was developed by Yagi and Wakao in 1959 for dispersion in a constant porosity packed tube, and it assumes a constant velocity in the radial direction of the tank.

4.9.3 Pressure Drop

Initially, it is assumed that there is no pressure drop across the regenerator. Once a solution has been calculated, the pressure drop is calculated using the Ergun equation (Ergun 1952).

$$\frac{dP}{dx} = \left(\frac{A\alpha\mu_f}{d_p^2}\right)vel + \left(\frac{B\beta\rho_f}{d_p}\right)vel^2 \tag{4.55}$$

Where

$$\alpha = \frac{\left(1-\varphi\right)^2}{\varphi^3} \quad and \quad \beta = \frac{1-\varphi}{\varphi^2} \tag{4.56}$$

The values of A and B can vary, but for smooth particles A is typically equal to 180, and B is equal to 1.8 (Kaviany 1995). Eq. (4.55) is used to calculate the pressure drop across each discretized section of the recuperator, and the total pressure drop ΔP is found using Eq. (4.57).

$$\Delta P = \sum_{i=1}^{M} \left(\frac{dP}{dx} \right)_i dx_i \tag{4.57}$$

From here, the pressure ratio reduction across the turbine $\left(\frac{\Delta P}{P} \right)_{tot}$ can be calculated using Eq. (4.58). In this equation, the subscript *low* refers to the low pressure side of the cycle, and the subscript *high* refers to the high pressure side of the cycle.

$$\left(\frac{\Delta P}{P} \right)_{tot} = \frac{\Delta P_{low}}{P_{low}} + \frac{\Delta P_{high}}{P_{high}} \tag{4.58}$$

4.10 Material Properties

There are several materials that can be used to create the bed of packed spheres; a comparison can be found in Table 4.1 below.

Table 4.1: Comparison of various materials for use as packed bed material

	AISI 316 SS	Ti6Al4V	Al2O3	SiC
Melting Temp [C]	1385	1630	2054	2700
Density [kg/m^3]	7969	4429	3957	3220
Conductivity [W/m-K]	15.96	8.288	25.07	77.5
Cost [$/kg]	4.00	20.00	11.00	8.00

316 stainless steel (316 SS) is the material currently used in Sandia's recuperator (Pasch, 2012). Ti6Al4V is a lightweight titanium alloy that can withstand extreme temperatures. Aluminum oxide (Al_2O_3) and silicon carbide (SiC) are ceramics, which are often used in regenerators because of its high specific heat capacitance, which is ideal for the indirect heat transfer used in this type of device (Cox 1950).

Since the size of the regenerator can vary, the capacitance ratio $\frac{C_r}{C_f}$ is calculated to compare the capacitance of a variety of potential materials (Figure 4.9). The equations for the

capacitance of the fluid C_f and the capacitance of the material C_r are defined in Eq. (4.59) and (4.60) below.

$$C_f = m_f\ c_p = \varphi\ A_c\ \rho_f\ c_p \tag{4.59}$$

$$C_r = m_r\ c_r = (1-\varphi)\ A_c\ \rho_r\ c_r \tag{4.60}$$

The area in Eq. (4.59) and (4.60) cancels out when used in the capacitance ratio.

$$\frac{C_r}{C_f} = \frac{(1-\varphi)\ \rho_r\ c_r}{\varphi\ \rho_f\ c_P} \tag{4.61}$$

Since the density and specific heat of CO_2 are highest near the critical point, this is also where the system has the highest potential for large energy storage in the fluid. As a result, the capacitance ratio is calculated at a pressure of 10 MPa.

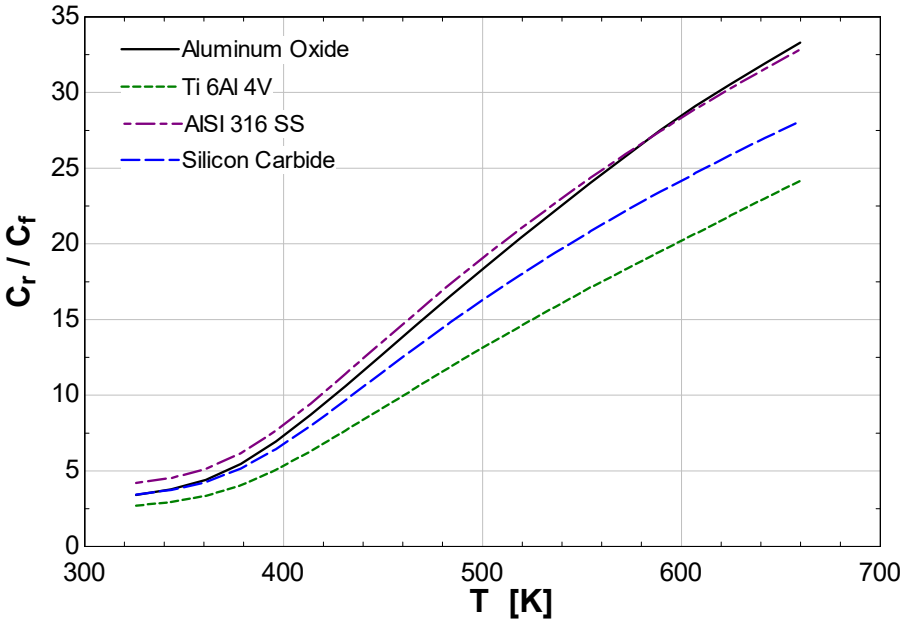

Figure 4.9: Capacitance ratio at various temperatures for possible packed bed materials. Pressure is at 10 MPa.

Figure 4.9 shows that Al_2O_3 and 316 SS have the two highest capacitance ratios. Between these two materials, Al_2O_3 is lighter, but more expensive; as a result, 316 SS is used for the material in the packed bed. The properties of 316 SS are taken from EES (Klein, 2014).

4.11 Tank Stresses

The tanks are assumed to be made of 316 SS. The equations for stress within a pressure vessel are used to calculate the transverse, radial, and lateral stresses within the tank walls.

$$\sigma_t = \frac{P_i r_i^2 - P_o r_o^2 - \frac{r_i^2 r_o^2 \left(P_o - P_i\right)}{r^2}}{r_o^2 - r_i^2} \tag{4.62}$$

$$\sigma_r = \frac{P_i r_i^2 - P_o r_o^2 + \frac{r_i^2 r_o^2 \left(P_o - P_i\right)}{r^2}}{r_o^2 - r_i^2} \tag{4.63}$$

$$\sigma_l = \frac{P_i r_i^2}{r_o^2 - r_i^2} \tag{4.64}$$

In Eq. (4.62)−(4.64), σ_t represents the transverse stress, σ_r represents the radial stress, and σ_l represents the longitudinal stress. The subscript *i* refers to the inside of the tank, and the subscript *o* refers to the outside of the tank. Once calculated, these stresses are used to find an equivalent von Mises stress σ'.

$$\sigma' = \sqrt{\frac{\left(\sigma_r - \sigma_t\right)^2 + \left(\sigma_t - \sigma_l\right)^2 + \left(\sigma_l - \sigma_r\right)^2}{2}}\,. \tag{4.65}$$

ASME pressure vessel codes state that the factor of safety, which is defined in Eq. (4.66), must be greater than or equal to 4.

$$\frac{\sigma'}{S_{uts}} \geq 4 \tag{4.66}$$

The variable S_{uts} refers to the ultimate tensile strength of 316 SS. To find the outer dimensions of the tank, an initial wall thickness th is used to calculate the wall stresses. This wall thickness is then adjusted until the factor of safety is greater than 4. The wall thickness can be used to calculate the outer radius of the tank, which in turn can be used to calculate the total tank volume.

$$r_o = r_i + th \tag{4.67}$$

$$Vol_{tank} = \pi \left(r_o^2 - r_i^2 \right) L \tag{4.68}$$

5 Regenerator Design

5.1 Design Method

When designing a regenerator based on its performance, the effectiveness, mass flow rate, and pressure ratio reduction across the turbine are constrained. The porosity of the bed is fixed at 0.37 based on the packing properties of spheres. The length and radius are fixed by the pressure drop and the heat transfer rate; however, these two variables are linked, which means that a separate parametric study must be completed to determine the correct length and radius combination that will match the desired performance. First, the pressure ratio reduction and effectiveness are calculated using the methods outlined in Sections 4.4 and 4.9.3 for a range of length and radii. A general trend of the results can be found in Figure 5.1 and Figure 5.2.

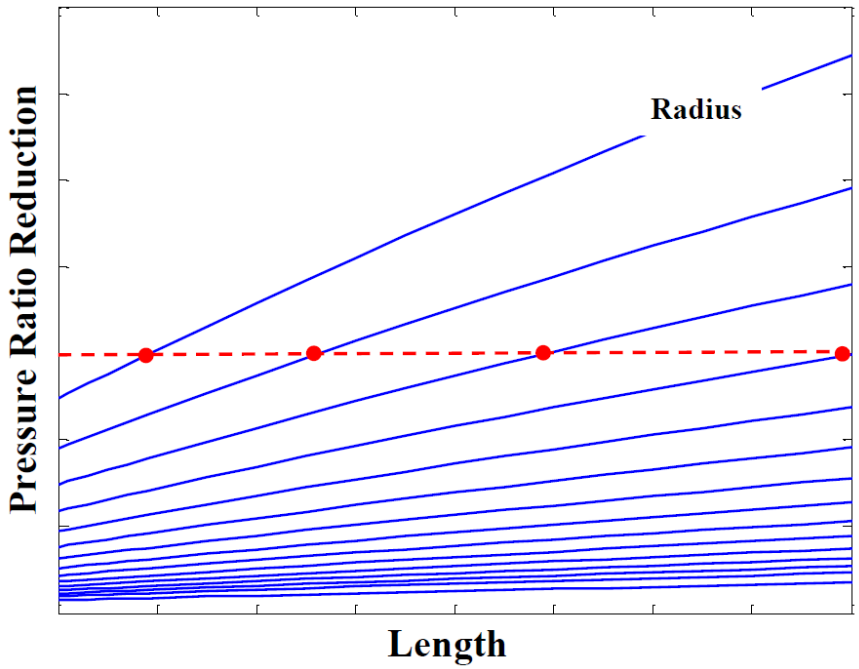

Figure 5.1: Diagram of pressure ratio reduction vs length for various radii. The red line represents the desired reduction across the turbine.

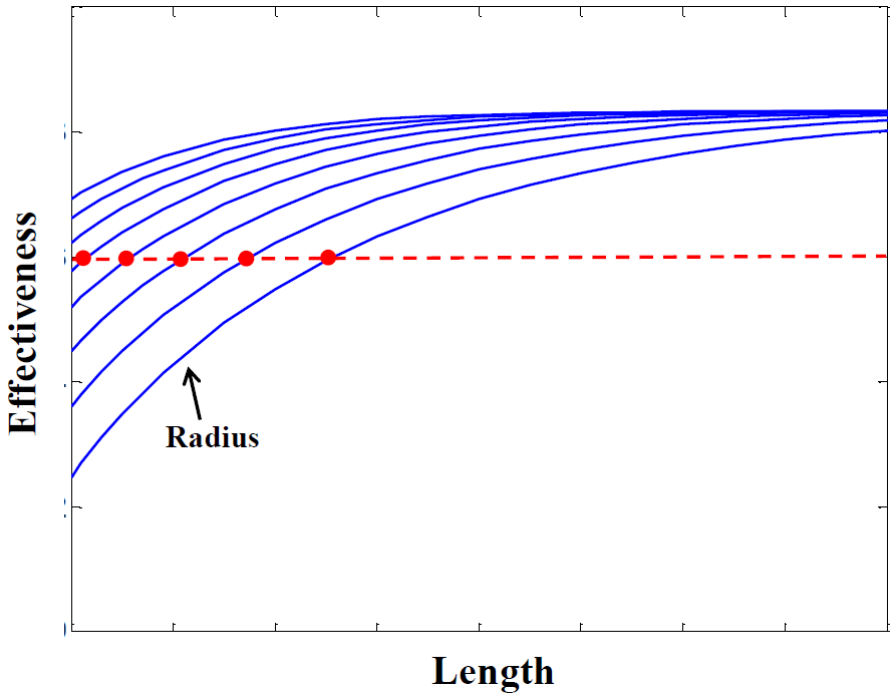

Figure 5.2: Diagram of effectiveness vs length for various radii. The red line represents the desired effectiveness.

The blue lines in Figure 5.1 and Figure 5.2 are lines of constant radius, and the red lines represent the desired pressure ratio reduction and effectiveness, respectively. The red dots indicate the pairs of length and radii that will produce those values. Comparing these pairs to each other will determine which combination results in the correct pressure ratio reduction and effectiveness (Figure 5.3). This is done using the FZERO function in MATLAB, which determines the root of a nonlinear function. The coordinates on the constant pressure ratio reduction line are subtracted from the coordinates on the effectiveness line, and the FZERO command determines where that difference is zero. This is where the two lines intersect, and these coordinates are the length and radius that produce the desired performance in the regenerator.

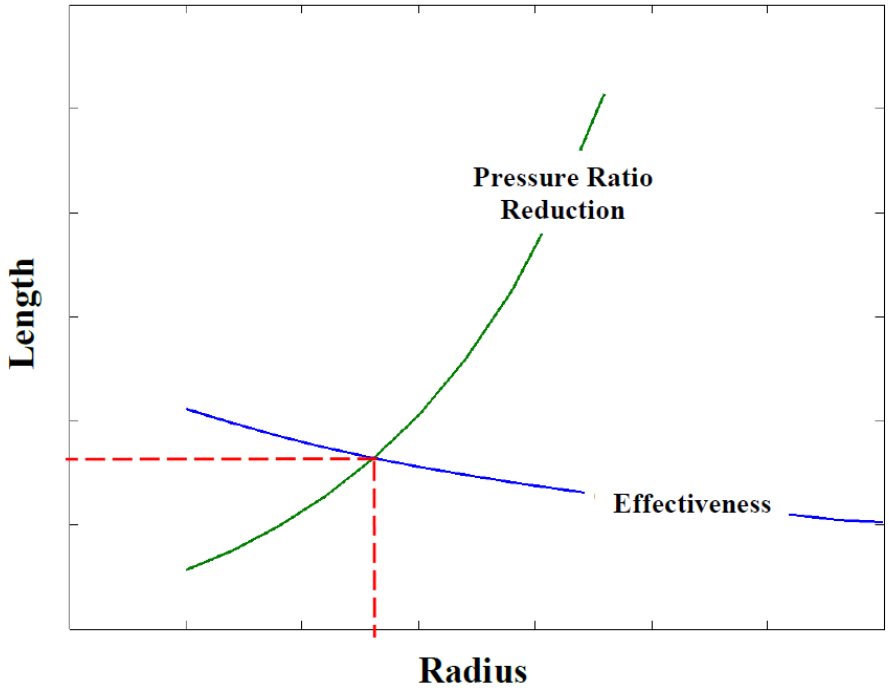

Figure 5.3: Diagram of length vs radius for the desired effectiveness and pressure ratio reduction. The two lines intersect at the desired length and radius.

Since the length, cross sectional area, and porosity are all fixed, the only free parameters are the cycle time and the size of the spheres in the packed bed. The effects of these parameters will be discussed further in Sections 5.2 and 5.4.

5.2 Effect of Sphere Diameter

To determine the effects of sphere diameter on regenerator size, the model was used to design regenerators with sphere sizes ranging from 0.793 mm to 6.35 mm (1/32" to 1/4") diameters. Each sphere diameter has its own "design space" that illustrates the relationship between geometry, effectiveness (Section 4.4), and pressure ratio reduction (Section 4.9.3). The design space for a regenerator with 0.793 mm (1/32") diameter spheres can be seen in Figure 5.4.

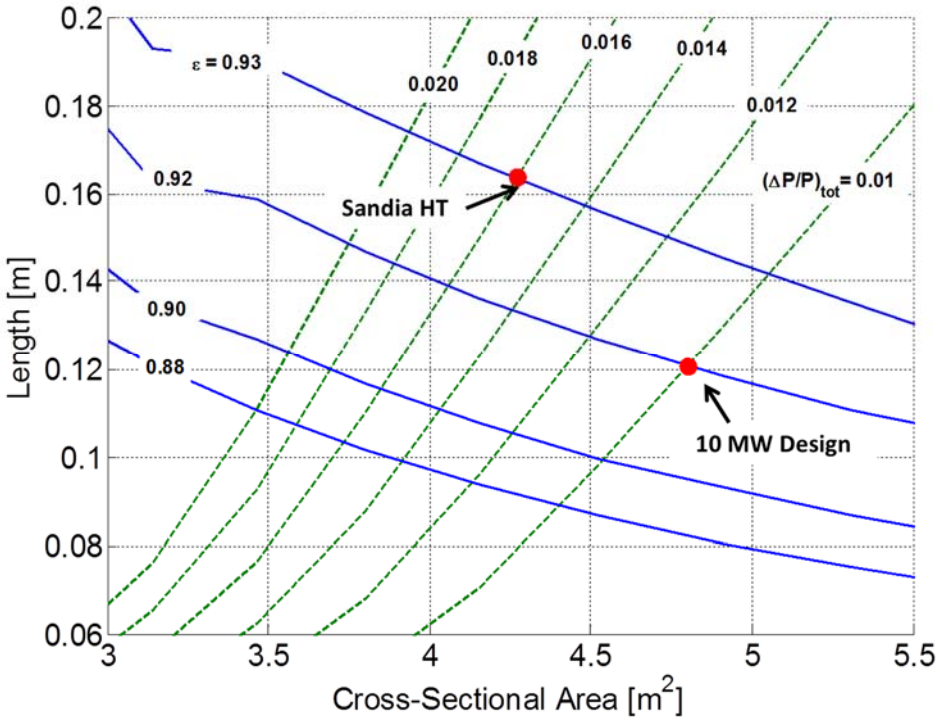

Figure 5.4: Design space for 0.793 mm spheres. The dashed lines represent lines of constant pressure ratio reduction, and the solid lines represent lines of constant effectiveness.

The solid blue lines are lines of constant effectiveness, and the green dashed lines are lines of constant pressure ratio reduction. The remaining design spaces can be found in Appendix A.

The two red dots in Figure 5.4 represent two specific design points. "Sandia HT" refers to the high-temperature recuperator used by Sandia (Section 3.2), which has been scaled to perform in a 10 MW cycle. "10 MW Design" refers to the recuperator designed in Chapter 3. A comparison of these two recuperators with their respective regenerators can be found in Table 5.1.

Table 5.1: Comparison of recuperator and regenerator volume and cost.

	10 MW Recuperator Design	Regenerator
effectiveness	0.92	0.92
pressure ratio reduction	0.01	0.01
volume [m³]	2.58	1.152
Cost	$ 1,700,000	$23,000

	Sandia HT Recuperator	Regenerator
effectiveness	0.93	0.93
pressure ratio reduction	0.016	0.016
volume [m^3]	3.152	1.445
Cost	$ 1,800,000	$29,000

The volume of the regenerator is twice as large as the volume calculated from Figure 5.4 because it required two tanks to operate, and the design space is for a single tank. There is a 55% reduction in volume when switching to a regenerator for the 10 MW cycle, and a 54% reduction in volume for Sandia's setup. A plot of this volume reduction at different sphere sizes can be found in Figure 5.5.

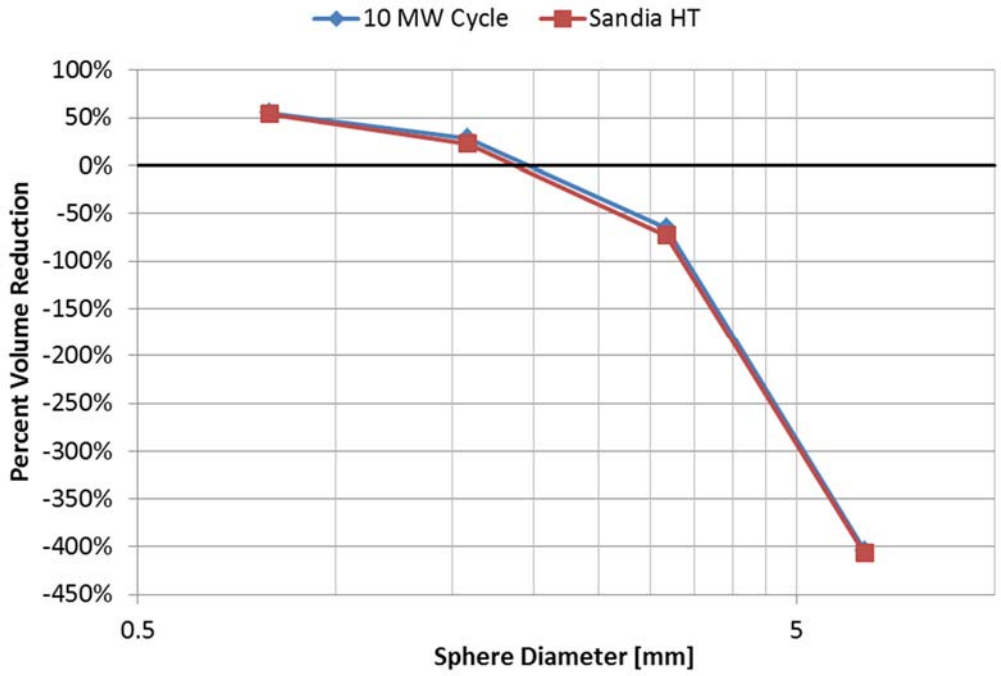

Figure 5.5: Graph of the percent reduction in volume between the recuperator and regenerator at various sphere sizes.

In Figure 5.5, a positive percentage means that the regenerator volume is smaller than the recuperator volume, and a negative percentage means that the regenerator volume is larger. As the sphere size increases, the percent reduction decreases, and at 3.17 mm (1/8") diameter

spheres the regenerator volume is larger than that of the recuperator. This suggests that spheres used should be no larger than 1.59 mm (1/16") across if regenerator size is an issue.

In Table 5.1, the cost of the regenerator is based on the price of the packed bed material, while the cost of the recuperator is based on Sandia's cost estimates (Wright, 2011). Assuming that the cost of material is a significant portion of the regenerator's cost, there is a 98% reduction in cost between the recuperator and the regenerator. A plot of cost reduction at different sphere sizes can be found in Figure 5.6.

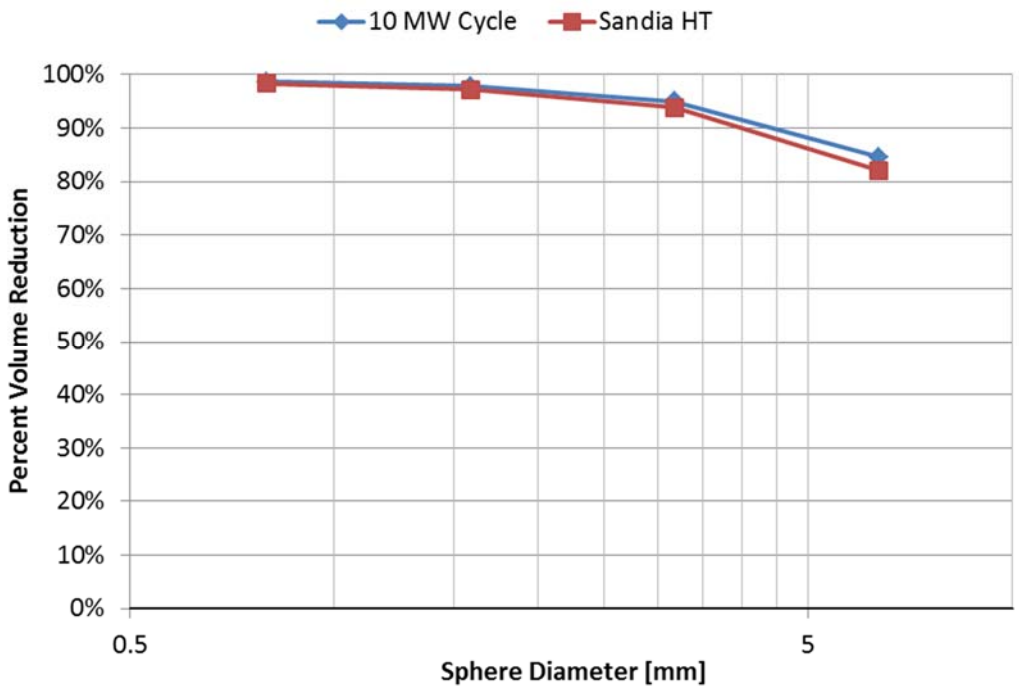

Figure 5.6: Graph of the percent reduction in cost between the recuperator and regenerator at various sphere sizes.

Figure 5.6 shows that regardless of sphere size, a regenerator can have upwards of 80% reduction in cost. This percentage is optimistic because the cost of manufacturing will have an effect on the price, but this cost will not be nearly as significant as in the recuperator.

5.3 Multi-Tank System

While the regenerator has a total volume that is smaller than the recuperator, the overall dimensions of this design is impractical. For the 10 MW design from Chapter 3, for example, each tank is about 2.5 m (7 ft) across. Using the stress analysis outlined in Section 4.11, the wall thickness needs to be at least 0.61 m (2 ft) to withstand the pressures within the system. In addition to a large diameter and thick tank walls, the length of the tank is only 0.12 m (4.7 in), making this dimensions unfeasible for a real life situation. Instead of using two tanks to build the regenerator, a better method would be to divide the cross-sectional area of each tank into a series of smaller pipes that could better withstand those pressures.

To determine what kind of pipes can withstand the pressures in the system, a stress analysis was done to determine the required wall thickness at various pipe diameters. This analysis was then compared to commercially available 316 SS piping in Figure 5.7.

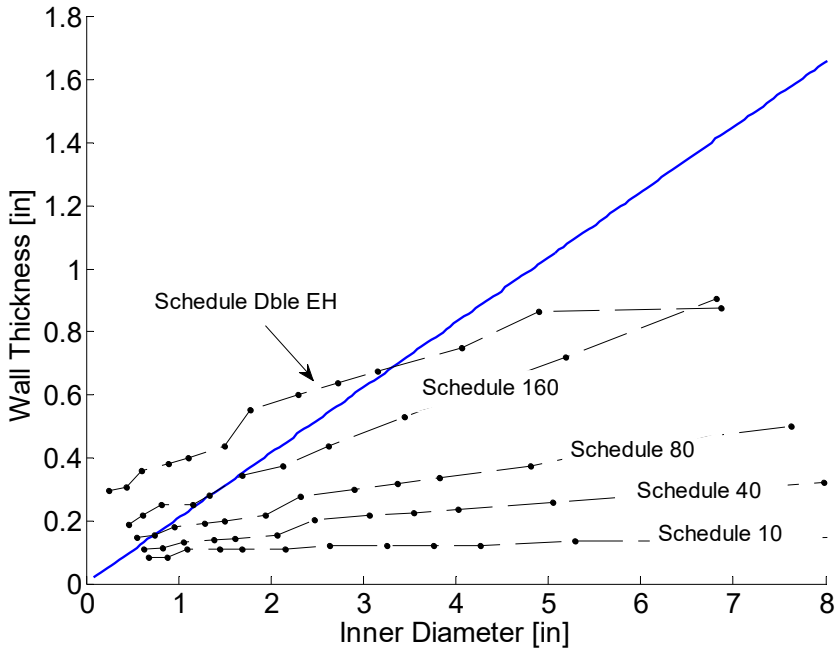

Figure 5.7: Graph of wall thickness vs inner diameter for various pipe schedules. The blue line represents the maximum pipe size that meets safety requirements.

In Figure 5.7, the solid blue line represents the maximum pipe size that can be used, and the dotted black lines represent the available sizes for different pipe schedules. Everything above and to the left of the solid line can be used to build a regenerator in a 10 MW system. The largest pipe size that meets these requirements, size 3 ½ Schedule Dbl EH, is used to estimate how many pipes are needed for the required performance of the regenerator. This is done by dividing the total cross-sectional area needed by the cross-sectional area of the pipe. The results are shown in Figure 5.8 below.

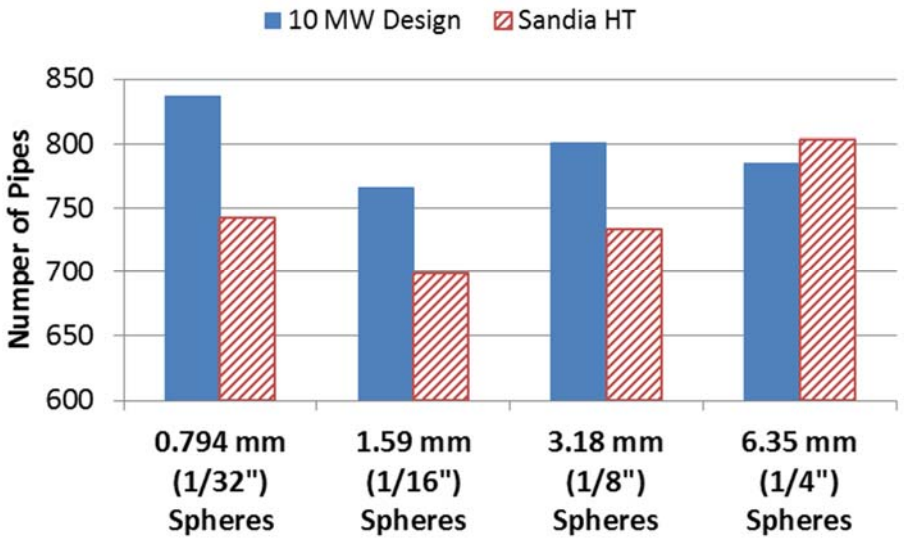

Figure 5.8: Graph of number of pipes vs sphere diameter for 316 SS pipes (Size 3 ½ Schedule Dbl EH).

This figure shows that between 700 and 850 pipes are needed to replace one tank, depending on the design. Since the regenerator is made up of two tanks, the total number of pipes is double this amount. At smaller sphere sizes the scaled Sandia regenerator, which has both a higher effectiveness and higher pressure ratio reduction across the turbine (Figure 5.4), requires fewer pipes that the 10 MW design. This suggests that increasing these parameters can increase the simplicity of the multi-tank design by reducing the required number of pipes.

5.4 Leakage Model

The current model does not take into account any leakages, which could have a significant effect on the regenerator design. In 2005, Skiepko and Shah suggested using a two-regenerator method of modelling to account for this leakage. The internal regenerator is considered the "ideal" regenerator, and is similar to the model described in previous chapters. The leakages are then modeled in the external "actual" regenerator (see Figure 5.9).

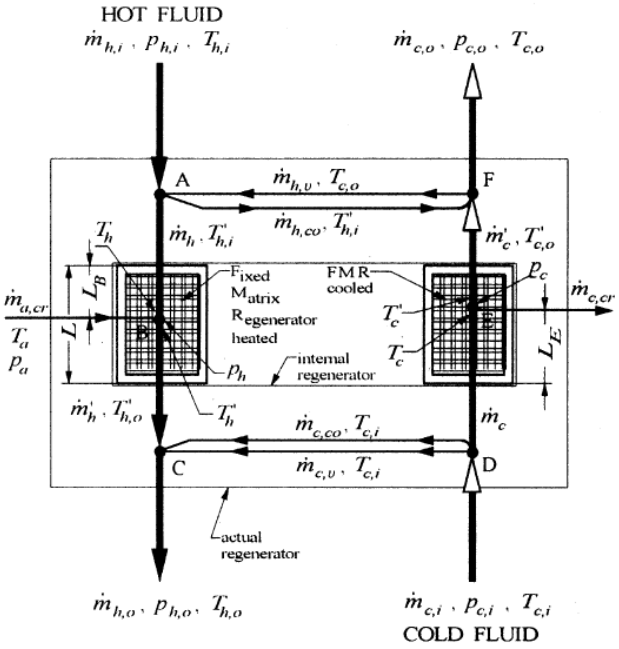

Figure 5.9: Diagram of regenerator model with leakage (Skiepko, 2005).

There are three types of leakage taken into account in Shah's model. The first is pressure leakage, which occurs as the valves switch the hot and cold streams. This leakage always occurs from high to low pressure; in this case it always leaks from the cold to the hot flow. The valve leakage rate depends on the discharge coefficient and the valve area, both of which depend on the type of valve being used.

$$\dot{m}_{c,v} = C_d \, A_{c,v} \sqrt{2 \rho_{c,i} \left(\rho_{c,i} - \rho_{h,o} \right)} \tag{5.1}$$

$$\dot{m}_{h,v} = C_d \, A_{h,v} \sqrt{2 \rho_{c,o} \left(\rho_{c,o} - \rho_{h,i} \right)} \tag{5.2}$$

In Eq. (5.1) and (5.2), $\dot{m}_{c,v}$ and $\dot{m}_{h,v}$ refer to the leakage mass flow rates across the valves during the cold-to-hot blow and the hot-to-cold blow, respectively. The subscript *i* refers to the fluid entering the tank, and the subscript *o* refers to fluid exiting the tank. The variable C_d is a discharge coefficient, and $A_{c,v}$ and $A_{h,v}$ refer to the area of the valve; both of these depend on the type of valve that is used.

The second form of leakage is known as crack leakage, which occurs across the matrices within the internal regenerator. This type of leakage only occurs in certain applications. Since the current design assumes that the matrices are housed in separate tanks, this leakage can be neglected.

The final type of leakage is from carryover, which is defined as the interstitial fluid that remains in the regenerator matrix and pipes at the end of a period. This fluid is removed when the new stream flows through the matrix, but the net result is a leakage loss in the regenerator.

$$\dot{m}_{c,co} = \frac{A_{fr} \, \varphi}{t_b} \sum_{i=1}^{M} \rho_{i,2*N} \, dx + \frac{\Delta Vol_{pipe} \, \rho_{c,in}}{t_b} \tag{5.3}$$

$$\dot{m}_{h,co} = \frac{A_{fr} \, \varphi}{t_b} \sum_{i=1}^{M} \rho_{i,N} \, dx + \frac{\Delta Vol_{pipe} \, \rho_{h,o}}{t_b} \tag{5.4}$$

In Eq. (5.3) and (5.4), $\dot{m}_{c,co}$ and $\dot{m}_{h,co}$ refer to the carryover mass flow rates during the cold-to-hot blow and the hot-to-cold blow, respectively. The first term in the equation is the mass of fluid that is sitting in the tank at the end of the cycle, and the second term is the mass of

fluid sitting in the pipes between the tank and the valves. Both of these terms are divided by the cycle time to determine the mass flow rate.

By performing a mass and energy balance at each of the lettered points in figure 5.8, an adjusted mass flow rate and temperature can be used to model the ideal regenerator. The exit temperature of the ideal regenerator is then modified again, resulting in mass flow rates and temperatures that account for all forms of leakage.

5.4.1 Effects of Carryover and Cycle Time

This model assumes that carryover is the main form of leakage in the regenerator, and that the leakage across the valve is negligible in comparison. It is also assumed that the carryover from the tanks is significantly larger than the pipe carryover, which reduces Eq. (5.3) and (5.4).

$$\dot{m}_{c,co} = \frac{A_{fr}\,\varphi}{t_b}\sum_{i=1}^{M}\rho_{i,2*N}\,dx \tag{5.5}$$

$$\dot{m}_{h,co} = \frac{A_{fr}\,\varphi}{t_b}\sum_{i=1}^{M}\rho_{i,N}\,dx \tag{5.6}$$

For the 10 MW cycle outlined in Chapter 3, Eq. (5.5) and (5.6) were used along with Shah's method to model the regenerator with carryover. A plot of effectiveness versus cycle time for this regenerator can be found in Figure 5.10.

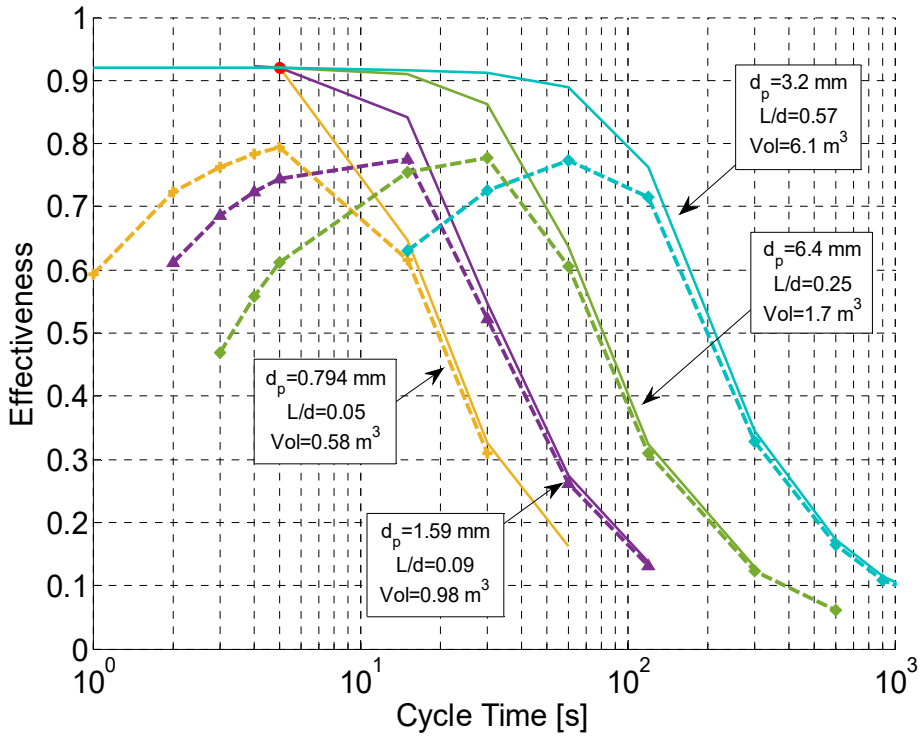

Figure 5.10: Plot of effectiveness versus cycle time for various sphere sizes. The solid lines represent an ideal regenerator with no carryover, while the dashed lines represent a regenerator with carryover taken into account.

In Figure 5.10, each set of solid and dashed lines correspond to a tank filled with different sized spheres; the yellow lines on the far left correspond to the 0.793 mm spheres, and the blue lines on the far right correspond to the 6.35 mm spheres. The solid lines show the effectiveness of the ideal case, which neglects carryover, and the dashed lines represent the effectiveness of a regenerator with carryover taken into account. At a large cycle time, the leakage in the regenerator is small, and the effectiveness of the regenerator with carryover is similar to the ideal case. As the cycle time decreases, however, the leakage increases until it becomes the dominating factor in performance, and the effectiveness begins to decrease again. This behavior suggests that there is an optimal cycle time at which a maximum heat transfer rate can occur. It is important to note that even at this optimum point, the effectiveness of the regenerator is about 13% lower than the ideal case, which suggests that

carryover and other leakages need to be accounted for when designing a regenerator for this type of system.

6 Conclusions and Recommendations

Printed circuit heat exchangers (PCHEs) are popularly used in supercritical CO_2 power cycles because of their compact size. But the diffusion bonding process makes the PCHE expensive, and operating in high temperatures and pressures means that the PCHE must be manufactured with high grade alloys, which only increases that cost. A fixed-bed regenerator, on the other hand, can be constructed using inexpensive materials and simple joint areas, which can significantly reduce cost.

If the sphere size is 1.59 mm (1/16") or smaller, there is at least a 30% reduction in volume compared to the recuperator, which means that the regenerator can benefit applications where space is an issue. Unfortunately, these geometries are impractical for a two-tank system in real life. Instead, the tanks need to be divided into smaller pipes. The number of these pipes depends on both the effectiveness and the pressure ratio reduction across the turbine. A higher effectiveness and higher pressure ratio reduction can reduce the number of pipes that are needed, which in turn decreases the complexity of a multi-tank system. An analysis that determines the effect of the regenerator's pressure drop and effectiveness on the cycle performance needs to be conducted to determine the appropriate combination of pressure ratio reduction and thermal effectiveness for a multi-tank system. An investigation should also be done into the types of pipes that are available. The pipes used in this analysis are 316 SS, but pipes made with a material that has higher stress resistance at high temperatures will further reduce the amount of pipes needed in the regenerator.

When comparing the size and cost of a regenerator and an equivalent recuperator in a 10 MW cycle, it is found that the regenerator can result in a significant reduction of cost, regardless

of the sphere size used in the packed bed. This is only a simple cost comparison because the cost of the regenerator only includes the material of the packed bed. A more in-depth analysis that includes other aspects of the system such as the pipes and the valves is needed for a more accurate comparison.

Carryover and other leakages are important when designing regenerators for S-CO2 power cycles. When including carryover in the regenerator design, the effectiveness of the regenerator decreases by at least 13%, depending on the cycle time. It also appears that the maximum effectiveness that can be achieved is limited when accounting for carryover; further investigation is needed to determine if this is the case. Other forms of leakage should also be studied, especially leakage across the valves. Examining which valves will produce the most leakage will help conclude what type of valve best fits this application.

.

7 References

Baek, S., Kim, J.-H., Jeong,S. & Jung,J. (2012). Development of highly effective cryogenic printed circuit heat exchanger (PCHE) with low axial conduction. *Cryogenics, 52*(7-9), 366-374.

Çhengel, Y. (2010). Gas Power Cycles. In *Thermodynamics: An Engineering Approach*. New York, NY: McGraw-Hill.

Cox, M. & Stevens, R. (1950). The regenerative heat exchanger for gas turbine power plant. *Proceedings of the Institution of Mechanical Engineers.*

Dostal, V. (2004). *A Supercritical Carbon Dioxide Cycle for Next Generation Nuclear Reactors*. (Doctoral Dissertation). Retrieved from http://dspace.mit.edu

Dyreby, J. et al. (2013, June). Modeling Off-Design and Part-Load Performance of Supercritical Carbon Dioxide Power Cycles. Proceedings of ASME Turbo Expo.

Efficiencies in Electricity Generation (2003, July). Retrieved from www.eurelectric.org

Ergun S.(1952), "Fluid Flow through Packed Column," Chemical Engineering Progress, Vol.48, No. 2, p. 125-127.

Feierabend, L. (2009) Thermal Model Development and Simulation of Cavity-Type Solar Central Receiver Systems (Master's Thesis). University of Wisconsin-Madison, Madison, WI.

Gonzo E., (2002) "Estimating Correlations for the effective thermal conductivity of granular materials", Chemical Engineering Journal, Vol.90, p. 299-302.

Handley, D., & Heggs, P. J. (1968). Momentum and heat transfer mechanisms in regular shaped packings. *Transactions of the Institution of Chemical Engineers and the Chemical Engineer*, 46(9), T251.

Hunter, L. (2010). CO2 flow measurement key in CCS schemes. powerengineeringint.com.

Ivenpah Project Facts (2013). Retrieved from *www.ivenpahsolar.com*

Juvinall, R. C., & Marshek, K. M. (2006). *Fundamentals of Machine Component Design.* (4th ed). John Wiley & Sons.

Kaviany M. (1995). Principles of Heat Transfer in Porous Media. Springer, New York.

Keller, C. (1978). Forty years of experience on closed-cycle gas turbines. Annals of Nuclear Energy 5 (8–10): 405–201.

Kim DE, Kim MH, Cha JE, Kim SO. (2008) Numerical investigation on thermal– hydraulic performance of new printed circuit heat exchanger model. *Nuclear Engineering and Design* 238(12):3269–76.

Klein, S.A. (2014). *Engineering Equation Solver (EES),* F-Chart software.

La Fleur Y. (1963) Description of an operating closed cycle helium gas turbine, ASME paper 63-AHGT-74.

Lake Side 1 and 2 Generation Facilities (2014). Retrieved from *www.pacificorp.com*

Le Pierres, R., et al. (2011, May) Impact of Mechanical Design Issues on Printed Circuit Heat Exchangers. Paper presented at the SCO2 Power Cycle Symposium, University of Colorado at Coulder – University Memorial Center, CO.

Li, Q., Flamant, G. et al. (2011). Compact heat exchangers: a review and future applications for a nes generation of high temperature solar receivers. *Renewable and Sustainable Energy Reviews,* 15(9), 4855-4875.

Nellis, G., & Klein, S. (2009). *Heat Transfer.* New York, NY: Cambridge University Press.

Ngo TL, Kato Y, Nikitin K, Tsuzuki N. (2006) New printed circuit heat exchanger with S-shaped fins for hot water supplier. *Experimental Thermal and Fluid Science* 30(8):811–9.

Nikitin K, Kato Y, Ngo L. (2006) Printed circuit heat exchanger thermal–hydraulic performance in supercritical CO2 experimental loop. *International Journal of Refrigeration* 29(5):807–14.

Pasch, J. (2013). *Closed Brayton Cycle Research Progress and Plans at Sandia National Labs* [PowerPoint Slides]. Retrieved from www.vcsi.org

Pasch, J., et. al., (2012) Supercritical CO2 Recompression Brayton Cycle: Completed Assembly Description (Sandia Report SAND2012-9546), Albuquerque: Sandia National Laboratories.

Pra F, Tochon P, Mauget C, Fokkens J, Willemsen S. (2008) Promising designs of compact heat exchangers for modular HTRs using the Brayton cycle. *Nuclear Engineering and Design* 238(11):3160–73.

Renewable Energy (2013). Retrieved from www.epa.gov

Seidel, W. *Model Development and Annual Simulation of the Supercritical Carbon Dioxide Brayton Cycle for Concentrating Solar Power Applications*. (Masters Thesis).

Skiepko,T. & Shah,R.K. (2005). Modeling and the effect of leakages on heat transfer performance of fixed matrix regenerators. *International Journal of Heat and Mass Transfer* 48 (2005) 1608–1632.

Solar in Demand (2012). Retrieved from www.energy.gov

The Compact Solution (N.A.). Retrieved from heatric.com

Titanium and Titanum Alloys (n.d.). Retrieved from www.asminternational.org

Tsuzuki N, Kato Y, Ishiduka T. (2007) High performance printed circuit heat exchanger. *Applied Thermal Engineering* 27(10):1702–7.

Van Meter, J (2008). *Experimental investigation of a printed circuit heat exchanger using supercritical carbon dioxide and water as heat transfer media* (Masters Thesis). Kansas State University, Manhattan, Kansas.

Wright, S.A., Conboy, T.M., & Rochau, G.E. (2001). *Overview of Supercritical CO2 Power Cycle Development at Sandia National Laboratories*. Presented at the University Turbine Systems Research Workshop, Columbus, Ohio.

Appendix A – Regenerator Design Space

0.794 mm (1/32”) Spheres

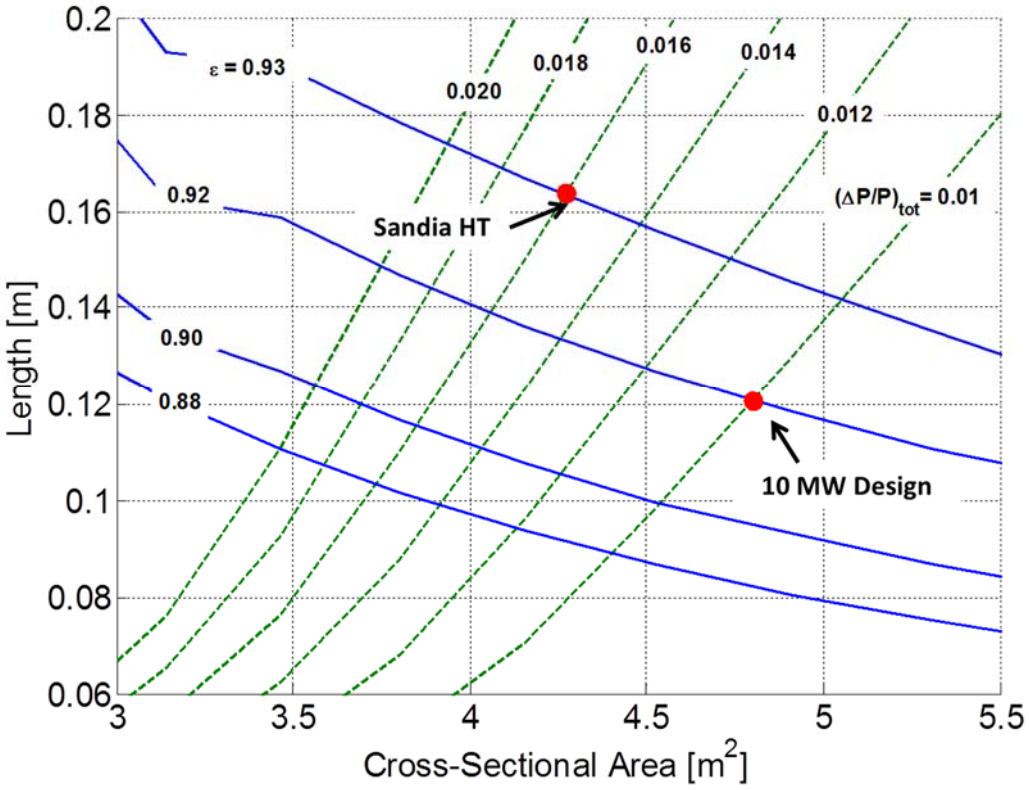

	10 MW Recuperator Design	Regenerator
effectiveness	0.92	0.92
pressure ratio reduction	0.01	0.01
volume [m³]	2.58	1.152
Cost	$ 1,700,000	$23,000

	Sandia HT Recuperator	Regenerator
effectiveness	0.93	0.93
pressure ratio reduction	0.016	0.016
volume [m³]	3.152	1.445
Cost	$ 1,800,000	$29,000

1.59 mm (1/16") Spheres

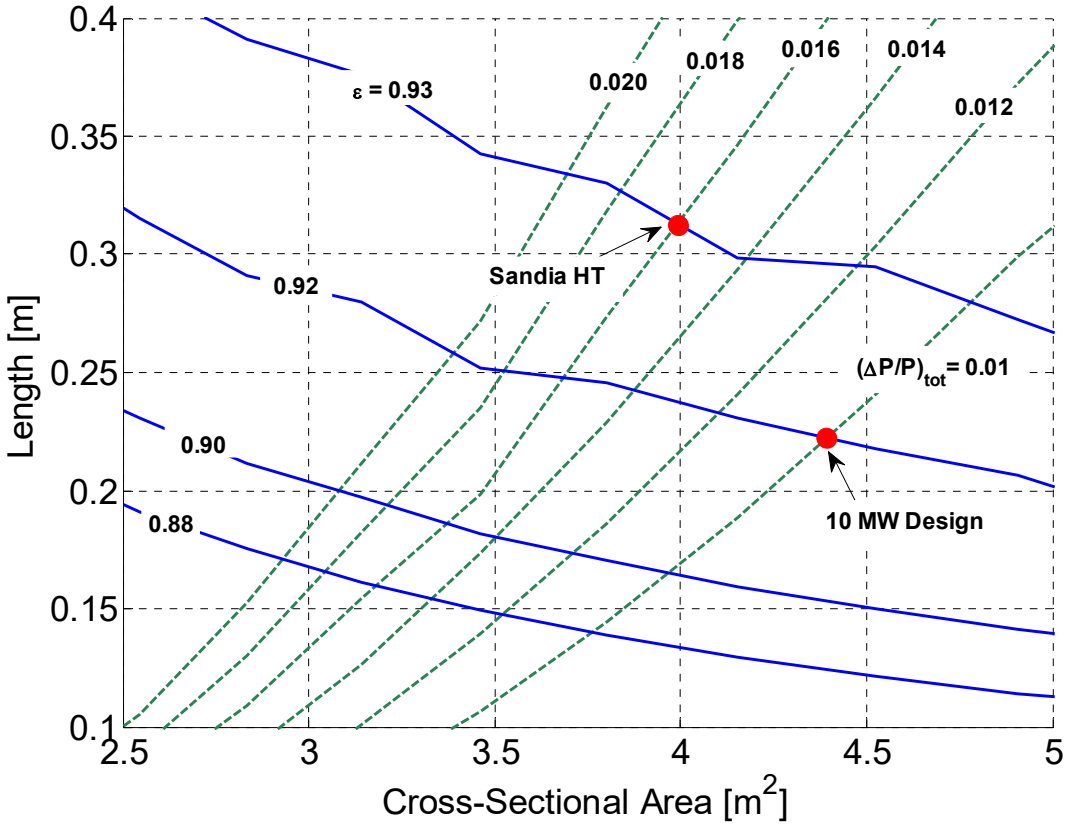

	10 MW Recuperator Design	Regenerator
effectiveness	0.92	0.92
pressure ratio reduction	0.01	0.01
volume [m^3]	2.58	1.85
Cost	$ 1,700,000	$37,300

	Sandia HT Recuperator	Regenerator
effectiveness	0.93	0.93
pressure ratio reduction	0.016	0.016
volume [m^3]	3.152	2.55
Cost	$ 1,800,000	$51,400

3.18 mm (1/8") Spheres

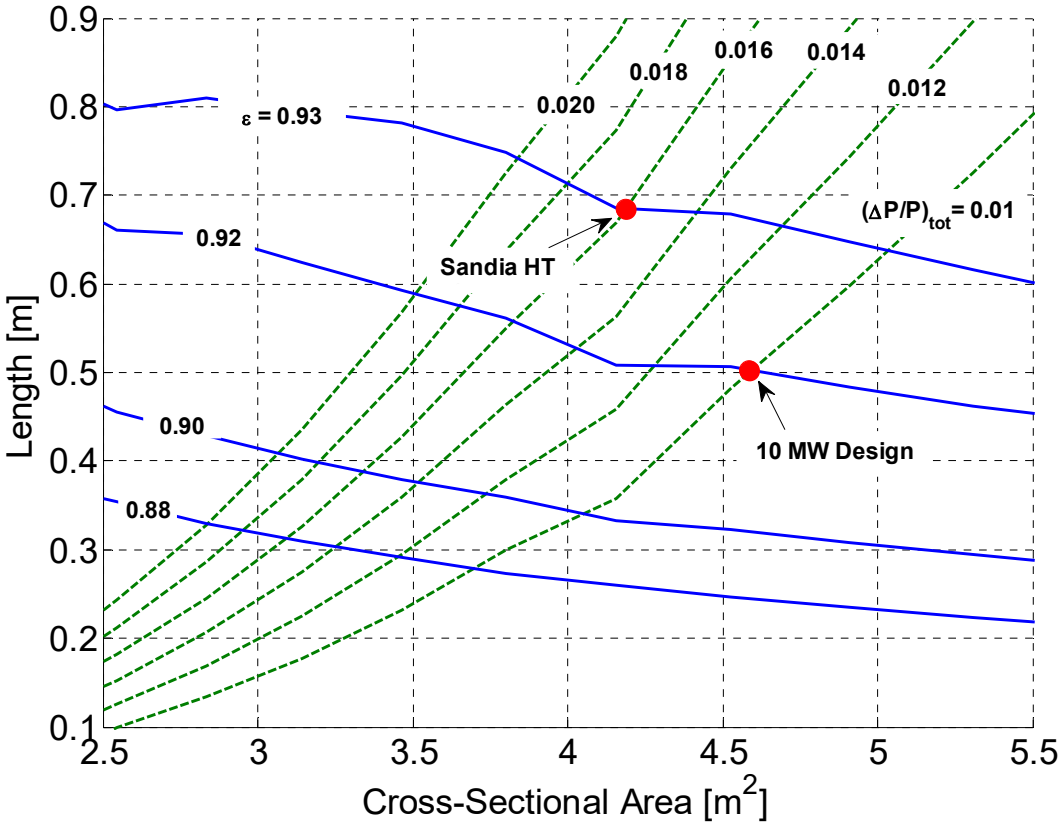

	10 MW Recuperator Design	Regenerator
effectiveness	0.92	0.92
pressure ratio reduction	0.01	0.01
volume [m^3]	2.58	4.25
Cost	$ 1,700,000	$85,700

	Sandia HT Recuperator	Regenerator
effectiveness	0.93	0.93
pressure ratio reduction	0.016	0.016
volume [m^3]	3.152	5.46
Cost	$ 1,800,000	$110,000

6.35 mm (1/4") Spheres

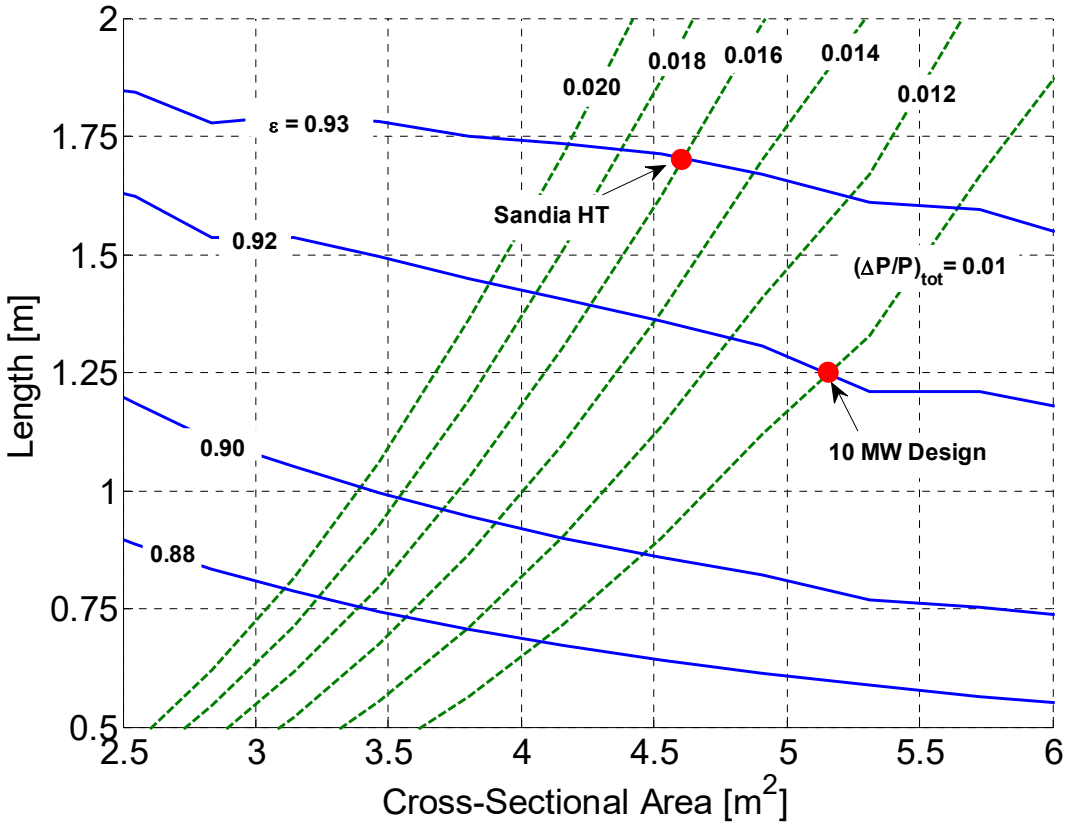

	10 MW Recuperator Design	Regenerator
effectiveness	0.92	0.92
pressure ratio reduction	0.01	0.01
volume [m^3]	2.58	13.0
Cost	$ 1,700,000	$262,000

	Sandia HT Recuperator	Regenerator
effectiveness	0.93	0.93
pressure ratio reduction	0.016	0.016
volume [m^3]	3.152	16.0
Cost	$ 1,800,000	$323,000

Appendix B – EES and MATLAB Code

All codes have been attached with the electronic version of this thesis.